Journal of Building Engineering 97 (2024) 110792

Contents lists available at ScienceDirect

Journal of Building Engineering

journal homepage: www.elsevier.com/locate/jobe

Biaxial shaking table testing of large-scale novel wireway vibration attenuation systems

Tran-Van Han [a,d], Sung Chan Kim [b], Jiuk Shin [c], Nguyen Huu Cuong [a,e], Kihak Lee [a,*]

[a] Deep Learning Architecture Research Center, Department of Architectural Engineering, Sejong University, 209 Neungdong-ro, Gwangjin-gu, Seoul 05006, Republic of Korea
[b] Sehong Inc, Ltd, 16, Tapsil-ro 58, Giheung-gu, Yongin-si, Gyeonggi-do, 17084, Republic of Korea
[c] Department of Architectural Engineering, Gyeongsang National University, Jinju-daero, Jinju-si, Gyeongsangnam-do 52828, Republic of Korea
[d] Faculty of Civil Engineering, Mien Trung University of Civil Engineering, Tuy Hoa and Danang, Viet Nam
[e] Department of Civil Engineering, Vinh University, Vinh 461010, Viet Nam

ARTICLE INFO

Keywords:
Pulley wireway
Shaking table testing
Non-structural components
Large-scale testing
Friction damper
Vibration attenuation

ABSTRACT

This research examines the seismic performance of large-scale pulley wireway systems subjected to four consecutive earthquakes using biaxial shaking table tests. A comparative analysis was conducted between novel lighting systems and a conventional raceway lighting system, each 20.50 m in length. Four specimens were tested: three pulley wireway systems and one conventional raceway lighting system, with varying suspended heights, support configurations, and cable pre-tension forces. The shaking table tests used time–history acceleration data to simulate artificial earthquakes per the ICC-ES AC156 standard. The results show that the novel lighting system exhibited superior earthquake performance and stability, outperforming the conventional system. Raising the suspension height increased seismic response and energy for the novel systems. Increasing cable tension improved stability under low seismic intensity but significantly increased seismic energy and response at high intensity. The absence of main hangers, combined with increased cable tension, reduced relative displacement but introduced instability at the ends and increased earthquake energy. These findings highlight the need to optimize suspension height, cable tension, and support configurations to enhance system resilience during earthquakes.

1. Introduction

In recent decades, significant progress has been made in seismic research for building structures, but the seismic performance of non-structural components (NSCs) has received little attention, resulting in extensive damage during earthquakes [1–5].

Lighting systems, among the most common NSCs, are crucial for building functionality and safety. Their failure during earthquakes can lead to substantial property loss and operational disruptions, especially in critical infrastructure like power plants, water treatment facilities, and hospitals, which must remain operational after an earthquake. For instance, during the 1994 Northridge Earthquake in California, lighting systems failed when fixtures were not properly secured with safety wires [6]. The 2001 Nisqually Earthquake in Washington caused partial ceiling and light fixture collapses, leading to a one-day closure of a terminal at Seattle-Tacoma International Airport [6]. Similarly, the 2010 Chile Earthquake caused significant non-structural damage, including to lighting systems, which led to the closure of Santiago International Airport [7]. In the 2013 Lushan Earthquake in China, damage

* Corresponding author.
E-mail address: kihaklee@sejong.ac.kr (K. Lee).

https://doi.org/10.1016/j.jobe.2024.110792
Received 28 May 2024; Received in revised form 23 August 2024; Accepted 17 September 2024
Available online 23 September 2024
2352-7102/© 2024 Elsevier Ltd. All rights are reserved, including those for text and data mining, AI training, and similar technologies.

Nomenclature

z	Height of structure with respect to grade, at point of attachment of the component.
h	Average building/structure roof height relative to the base elevation.
z/h	Height factor ratio.
R_p	Component response modification factor.
I_p	Component importance factor.
A_{FLX-H}	Horizontal spectral acceleration calculated for flexible components at z/h = 0.
A_{FLX-V}	Vertical spectral acceleration calculated for flexible components at z/h = 0.
A_{RIG-H}	Horizontal spectral acceleration calculated for rigid components at z/h = 0.
A_{RIG-V}	Vertical spectral acceleration calculated for rigid components at z/h = 0.
S_{DS}	Design spectral response acceleration at short period.
RRS	Required Response Spectrum.
TRS	Test Response Spectrum.
F_p	Design seismic force acting on the center of mass of non-structural elements.
F_a	The site coefficient.
S_s	The mapped Risk-Targeted Maximum Considered Earthquake spectral response acceleration parameter at short periods.

to suspended ceilings and lighting components was widespread in public buildings, from low-rise reinforced concrete (RC) frames to multi-story RC structures used for government offices, schools, and hospitals [8,9]. The 2016 Kumamoto Earthquakes in Japan caused damage even in buildings with seismic-resistant structures, including fallen furniture, light fixtures, and ruptured service pipes [10]. The 2018 Anchorage Earthquake in the USA resulted in extensive non-structural damage at Houston Middle School, particularly to unbraced suspended ceilings, lighting, ductwork, and other systems [11]. Significant damage to light fixtures was also reported during the 2018 Hualien Earthquake in Taiwan [12].

Despite the poor seismic performance of lighting systems observed in past earthquakes, research on their behavior under seismic loading remains limited. Qi et al. [13] studied the interaction between ceiling panels and electrical equipment, including lighting components, in multilevel suspended ceilings under seismic conditions. Qi et al. [14] conducted both experimental and analytical studies on the vibration properties of integrated ceiling systems, focusing on their interaction with nearby electrical equipment such as light fixtures. Additionally, Luo et al. [3] explored ways to improve the seismic performance of hook-on panel suspended ceilings by testing full-scale models with integrated light fixtures. Wang et al. [8] also tested suspended ceilings with light fixtures directly attached to the floor slab within a full-scale, single-span, single-story RC frame infilled with clay brick walls. Furthermore, Ryu and Reinhorn [15] conducted a series of full-scale shake table tests on fifteen different configurations of suspended ceiling systems, including lighting fixtures and air diffusers, to investigate the effects of various conditions posed by large-area ceiling systems.

Most studies have primarily examined the interaction of lighting components with suspended ceiling systems rather than complete lighting systems. The system-level experimental research, conducted by Han et al. [16–18], was limited to small-scale test specimens. Han et al. introduced a novel lighting support system featuring a pulley friction damper designed to reduce vibrations in raceway light fixtures during earthquakes. Shaking table tests on these shorter systems demonstrated that the friction dampers effectively reduced seismic energy and peak oscillations. Although these findings are promising, further investigation is required to assess the performance of this system in large-scale applications, where lighting systems are typically longer and have varying suspension heights.

This study aims to experimentally investigate the seismic performance of a large-scale innovative wireway vibration attenuation system designed for raceway light fixtures. Three pulley wireway systems and a conventional lighting support system of the same length were selected as test specimens. The input acceleration time histories were artificially generated to match the requirements of the ICC-ES AC156 standard [19], with varying amplitudes. The performance of the large-scale pulley wireway systems was evaluated under different conditions, including earthquake magnitudes, suspension heights, cable pre-tensions, and hanger types. The following sections detail the experimental outcomes.

2. Concept of the novel wireway vibration attenuation system

A raceway lighting system, illustrated in Fig. 5d, uses enclosed channels, or raceways, to house and protect electrical wires and cables. These raceways, typically mounted on ceilings or other surfaces using rod hangers, are critical in environments like office buildings, schools, and industrial facilities, where lighting failure during an earthquake could have severe consequences, necessitating enhanced seismic performance.

The novel pulley wireway system introduced in this study differs from traditional systems by incorporating a wireway vibration attenuation mechanism, as shown in Fig. 1. This system uses a cable wound around a pulley friction damper connected to a tension-adjusting device, depicted in Fig. 5(a-c). The tension-adjusting device features fixed and movable hooks. During installation, one

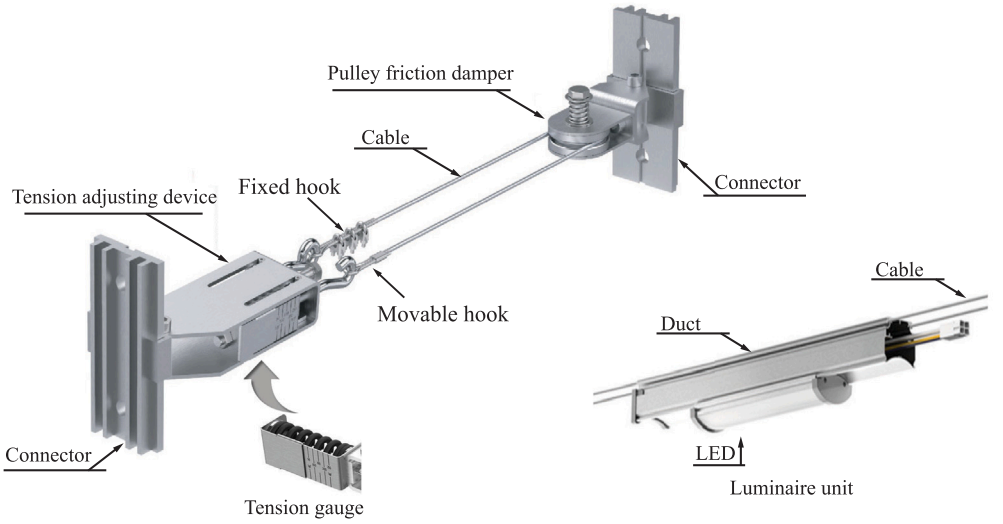


Fig. 1. Concept of the proposed vibration attenuation system.

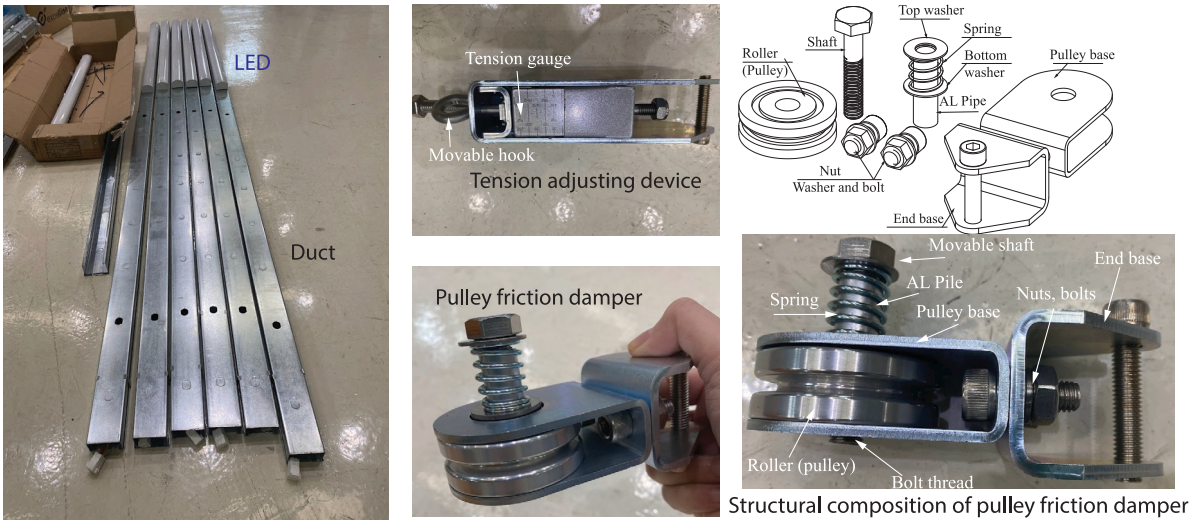


Fig. 2. The components of the pulley wireway system.

end of the cable is secured to the fixed hook, while the other end is looped around the pulley and attached to the movable hook. Cable tension is adjusted using a threaded mechanism that moves the hook along the cable to achieve the desired tension. The system's ends are anchored to the building's main structure using connectors, with the raceways supported by both the cable and steel cable hangers.

Fig. 2 illustrates the conceptual design of the pulley friction damper [16–18]. The damper dissipates seismic energy through four key friction interfaces:

1. Between the top surface of the pulley and the bottom washer,
2. Between the bottom surface of the pulley and its base,
3. Between the pulley and the aluminum (AL) pipe,
4. Between the cable and the pulley.

The damper's effectiveness is determined by the friction forces F_{f1} to F_{f4} generated at these interfaces, which are governed by the corresponding normal forces N_1 to N_4, as shown in Fig. 3.

For the interfaces between the pulley and the bottom washer (1) and between the pulley and its base (2), the normal forces N_1 and N_2 are controlled by a coaxial spring mechanism. This spring mechanism adjusts the spring force F_s through a movable,

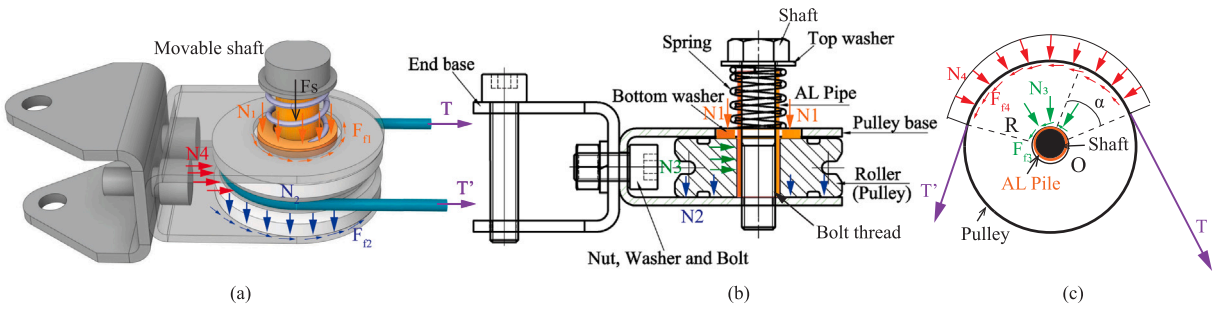


Fig. 3. Normal and friction forces acting on the friction surfaces of the pulley friction damper: (a) 3D view; (b) section view; (c) friction and normal forces generated on the pulley and aluminum pipe surfaces.

threaded shaft, thereby modulating the normal forces on these surfaces.

$$N_1 = N_2 = F_s = \Delta L \cdot k \tag{1}$$

where ΔL is the change in length of the spring, and k is the stiffness of the spring.

For the interfaces between the pulley and the aluminum pipe (3) and between the cable and the pulley (4), the normal forces N_3 and N_4 are determined by the tension in the cable. This tension is adjusted using a towing machine, and the resulting normal forces are calculated using the Euler–Eytelwein equation [20–22]:

$$N_3 = N_4 = T(\alpha) = \begin{cases} T' e^{\mu\alpha}, & \alpha \in \left[0, \frac{1}{\mu} \log \frac{T}{T'}\right] \\ T, & \alpha \in \left[\frac{1}{\mu} \log \frac{T}{T'}, \pi\right] \end{cases} \tag{2}$$

where T and T' are the axial forces at the two ends of the cable, with $T' \leq T$. The variable α represents the contact angle, and μ denotes the friction coefficient, which is 0.4 for steel-on-steel surfaces and 0.35 for steel-on-aluminum surfaces [23,24]. The cable tension T can be finely adjusted using the towing machine's adjustable hook, thereby optimizing the damper's ability to dissipate seismic energy.

3. Shaking table test

3.1. Shake table test frames

The seismic behavior of novel pulley wireway systems and a conventional raceway lighting system was investigated through shaking table tests conducted at the Earthquake Disaster Prevention Research Center, Pusan National University. This facility is equipped with a six-degree-of-freedom shaking table capable of simulating complex seismic events.

The shaking table tests included three key components: (a) two earthquake motion simulators (Shaking tables A and C), (b) a test frame composed of two identical steel stiff frames (labeled A and C) with a linking segment for seismic input transmission, and (c) four large-scale lighting system specimens. The frame, constructed from H-steel and U-steel sections, measured 21100 mm in length, 2960 mm in height, and 5000 mm in width, and was mounted on two 5000 × 5000 mm three-degrees-of-freedom shake tables. Structural stability was ensured using 32 M30 high-strength bolts at the base, connecting the frame to the shaking tables. Details of the test components and procedures are illustrated in Fig. 4.

3.2. Description of the test specimens

This study evaluated four large-scale specimens: three pulley wireway systems (Specimens 1–3) and one conventional raceway lighting system (Specimen 4), all with identical dimensions of 2600 mm in width and 20500 mm in length, and equipped with the same lighting units. These specimens are depicted in Fig. 5, with design parameters detailed in Table 1.

Specimens 1, 2, and 3 were suspended by a 4 mm diameter cable wound around a 60 mm pulley friction damper, attached to the ceiling using an 85×85 mm rectangular hollow connector with additional support from two bracing cables. Specimens 1 and 2 had two main hangers and three sub-hangers, while Specimen 3 used five sub-hangers. The main hangers were 4 mm diameter steel cables, and the sub-hangers were 2 mm. Suspension heights were 1000 mm for Specimen 1 and 1800 mm for Specimens 2 and 3, with cable tensions ranging from 60 to 150 kgf for Specimen 1, and fixed at 60 kgf for Specimen 2 and 200 kgf for Specimen 3.

Specimen 4 used ten steel rod sub-hangers, two three-axis rod hangers, and one two-axis rod hanger for structural support, all with a suspension height of 1800 mm. Despite being common in practice, this configuration is not certified for earthquake resistance according to AC156 [19] and SPS-F KOCED 0007-7419:2021 standards [25].

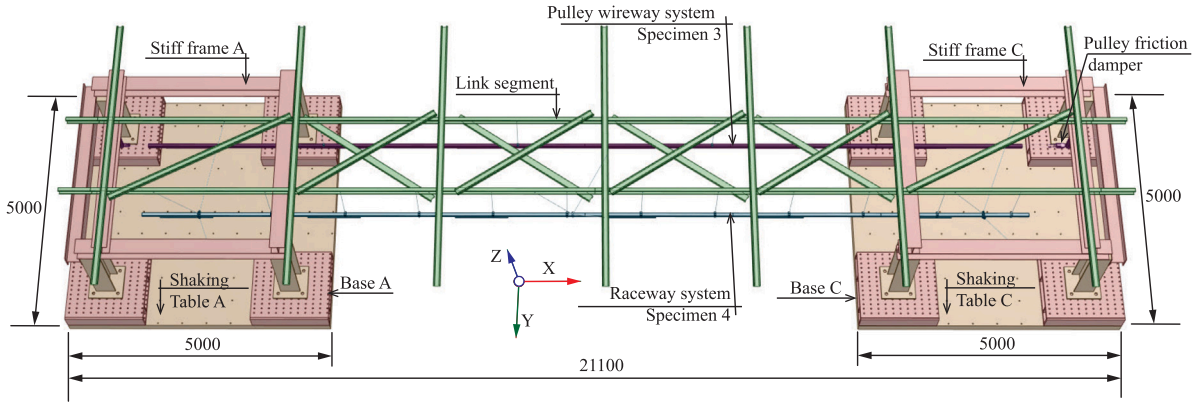


Fig. 4. Global view of the test setup.

Table 1
Parameters for designing the specimens.

Type	Specimen	Suspended height (mm)	Length(mm)	Support
Pulley	Specimen 1	1000	20 500	Sub-hangers + main-hangers + connectors
Wireway	Specimen 2	1800	20 500	Sub-hangers + main-hangers + connectors
	Specimen 3	1800	20 500	Sub-hangers + connectors
Conventional system	Specimen 4	1800	20 500	Sub-hangers + 3-axis and 2-axis main-hangers

Table 2
Mechanical characteristics of cable.

Item	Value	Units
Wire structure	7 × 7	–
Diameter	4	mm
Maximum load bearing	9.8	kN
Weight per unit length	0.066	Kg/m
Displacement (50 kgf tensile load)	0.7	mm
Modulus of elasticity	96 105	MPa

Table 3
Mechanical properties of all of the main components of the pulley wireway system.

Material	Density (g/cm^3)	Tensile strength (Ultimate) (MPa)	Tensile strength (Yield) (MPa)	Elongation at break (%)	Tensile modulus (GPa)	Poisson's ratio
AL6063	2.70	150	90	20	69	0.33
AL6061	2.70	310	276	12–17	68.9	0.33
SUS304	8.00	590	330	40	193	0.29
SS400	7.80	415	205	21	160	0.25

Materials used across these specimens included aluminized alloys (AL6063 for poles and ducts, AL6061 for pulleys), STS stainless steel for cables, and SS400 and SUS304-grade steel for structural supports. Mechanical characteristics and material qualities are detailed in Table 2 and Table 3, conforming to Korean Standard specifications.

3.3. Test setup and measuring instruments

The experimental setup is depicted in Fig. 4. Four specimens were tested in five separate steps, which were referred to as Steps 1–4 (Specimens 1 and 2), Steps 5 (Specimens 3 and 4).

Nine accelerometers and eight static linear variable displacement transducers (LVDTs) were employed to record acceleration and displacement responses along the longitudinal (X) and lateral (Y) directions for specimens and the steel frame during the experiments. LVDTs L1, L2, and L7 captured displacement at the base of table A, stiff frame A, and the link segment's midpoint, respectively. LVDT clusters L3 to L6 measured displacement for Specimens 1 and 2, and in Step 5, L4 and L6 were repositioned at the midpoint and endpoint of Specimen 3. Specimen 4 did not feature LVDT measurement.

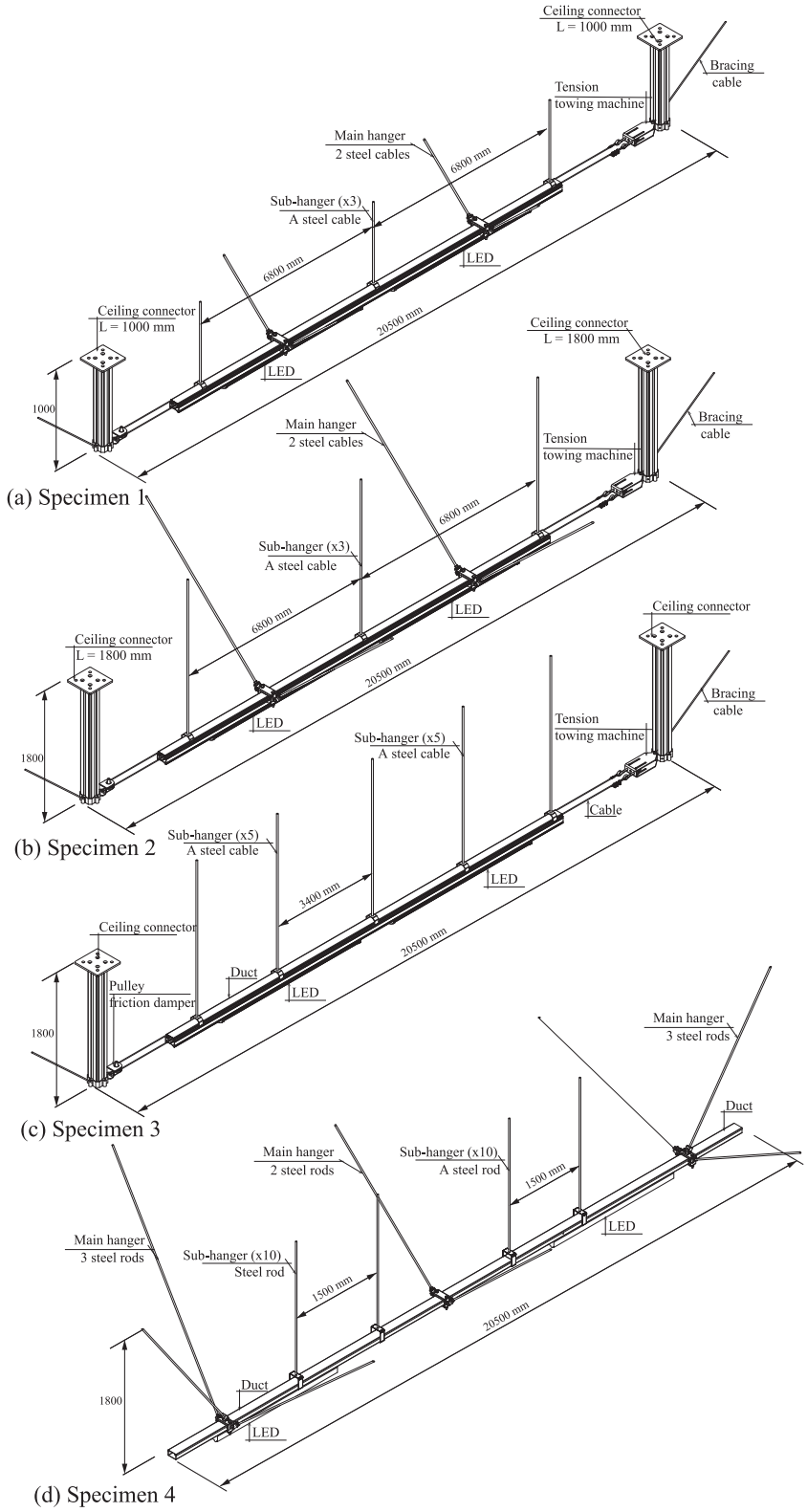
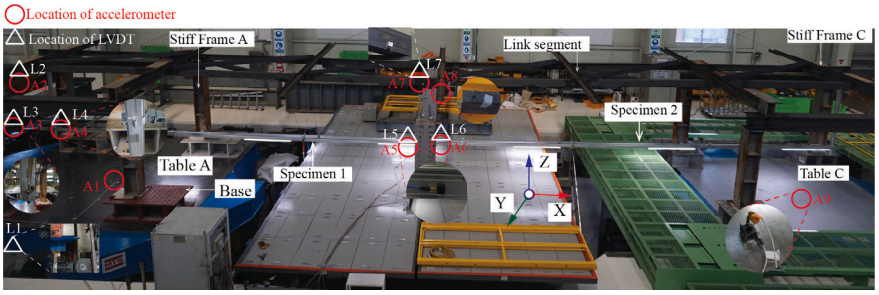
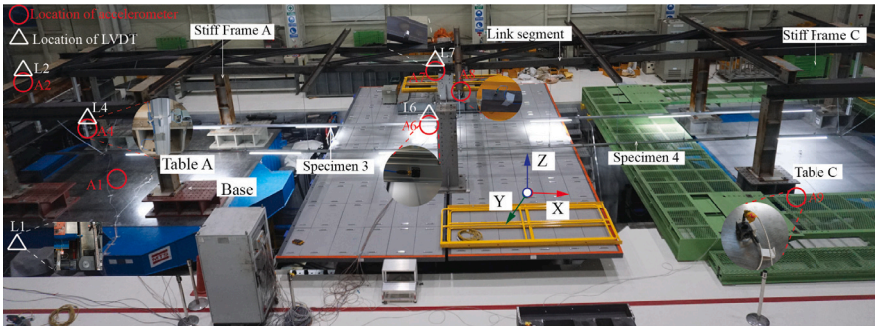


Fig. 5. Details of the Specimens 1,2,3 (the novel systems) and Specimen 4 (the conventional system).



(a) Step 1- Step 4 (Specimen 1 and Specimen 2 were tested).



(b) Step 5 (Specimen 3 and Specimen 4 were tested).

Fig. 6. Test set-up and measurement instrumentation.

Accelerometers A1 and A9 were strategically placed at the shaking table's base to generate the Test Response Spectrum (TRS) and verify input acceleration. A2, A7, and A8 were located at the top of the stiff frame and link segment to monitor high-level responses. Accelerometers A3 to A6 were used to assess the earthquake performance of Specimens 1 and 2, positioned at their midpoints and endpoints. For Specimen 3, A4 and A6 were adjusted to the midpoint and endpoint in Step 5, while Specimen 4 was not instrumented with accelerometers. For specific locations of the accelerometers and LVDTs in each step, refer to Fig. 6 and Table A.6 and Table A.7, respectively.

3.4. Input ground acceleration records

Shaking table tests were conducted according to the loading protocol recommended by ICC-ES-AC 156 [19], which has been widely used to evaluate the seismic performance of NSCs. The used seismic input was generated to satisfy the required response spectrum (RRS), which is the lowest seismic acceleration required to excite a target component as a function of the natural period or natural frequency. The RRS developed from the two parameters: the story height ratio (z/h), and the design spectral response acceleration at short periods S_{DS} [26–28]. The seismic parameters including the horizontal and vertical spectral acceleration for flexible and rigid components were used to calculate the RRS levels, as shown in Fig. 7.

The horizontal spectral acceleration for flexible A_{FLX-H} and rigid A_{RIG-H} components are computed as follows [19,25]:

$$A_{FLX-H} = S_{DS}\left(1 + 2\frac{z}{h}\right) \leq 1.6S_{DS} \tag{3}$$

$$A_{RIG-H} = 0.4S_{DS}\left(1 + 2\frac{z}{h}\right) \tag{4}$$

The vertical spectral acceleration of the flexible A_{FLX-V} and rigid A_{RIG-V} components are computed as follows [19,25]:

$$A_{FLX-V} = 0.67S_{DS} \tag{5}$$

$$A_{RIG-V} = 0.27S_{DS} \tag{6}$$

According to the Korean Design Standard [27] (KCSC 2019), the value of S_{DS} = 0.50 g under the assumptions of Site Class D (stiff) soil condition. In this study, AC156 input motion equivalent S_{DS} = 0.5 g was scaled from the value derived from standard using scaling factors of 100% (S_{DS} = 0.5 g) and 140% (S_{DS} = 0.7 g). Seismic parameters for required response spectrum are shown

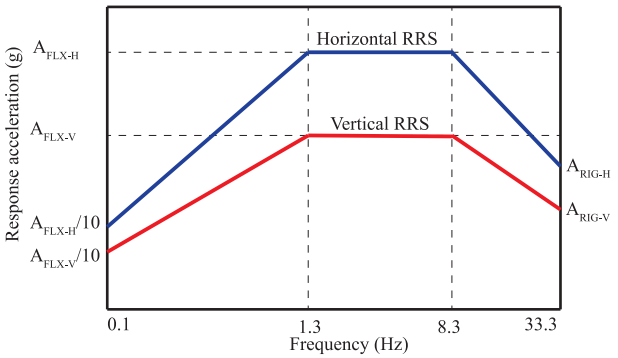


Fig. 7. Required response spectrum (AC156).

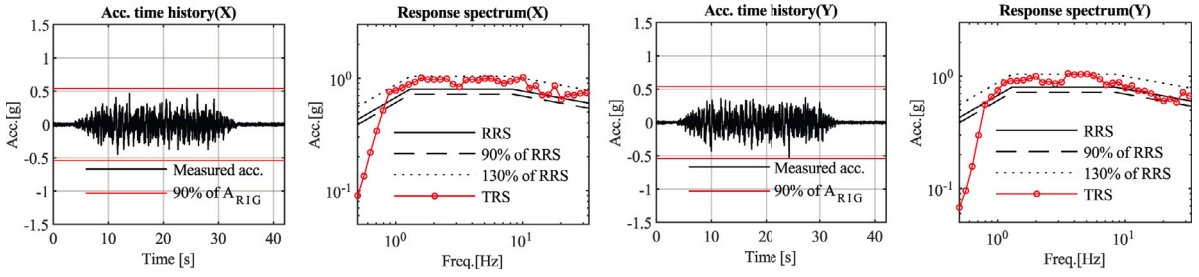


Fig. 8. Input acceleration time history corresponding to (S_{DS} = 0.5 g), TRS, RRS, upper and lower matching limits.

in Table A.8. A test plan is summarized in Table 4. The main biaxial shaking table tests for the four specimens were labeled as Test 3 (Step 1), Test 6 (Step 2), Test 9 (Step 3), Test 12 (Step 4), and Test 15 (Step 5).

Assuming specimens were attached to the top floor of structures, the study set z/h = 1.0. Fig. 8 shows the input acceleration time–history, its elastic response spectrum for damping value of 5%, namely the test response spectrum (TRS), the RRS, and the RRS scaled to 90 and 130%. The figure clear shows that the input acceleration met the ICC-ES AC156 and SPS-F KOCED 0007-7419:2021 requirements [19,25].

4. Test results and discussion

4.1. Damage observation

Specimens from a pulley wireway system and a conventional raceway lighting system underwent a series of visual inspections to assess damage following multiple earthquake simulations. Specimens 1 and 2 experienced four successive earthquakes, with magnitudes varying from 100% to 140% of AC156 standards, in both X and Y directions. Specimens 3 and 4 were each subjected to a single earthquake, as per AC156 guidelines (Fig. A.17, Fig. A.18 and Fig. A.19). Testing was continuous, with no replacements of damaged components, allowing for cumulative damage assessment. Significant findings include:

1. Bolts on main hangers of Specimens 1 and 2 loosened and deformed. Specimen 2 also had a detached connection bolt. No damage was noted in sub hangers or connectors.
2. Specimen 3 showed no damage at step 5, while Specimen 4 experienced bracket failures and noticeable system tilt due to loosened bolts.
3. Three specimens of the pulley wireway system displayed no significant structural damage or distortion after rigorous shaking table tests, suggesting robustness and operational consistency even under successive earthquakes, requiring minimal maintenance.
4. In contrast, the conventional raceway lighting system failed to meet functional requirements after a single earthquake, indicating a loss of balance and the need for extensive repairs.

The damage assessment compared the conventional raceway system to the novel pulley wireway system under similar testing conditions. Despite the pulley wireway system using only half the number of hangers and being subjected to more severe conditions, including four consecutive earthquakes with S_{DS} up to 0.7 g, it demonstrated superior performance. The pulley wireway system met all AC156 required criteria, whereas the conventional system failed after a single earthquake with S_{DS} = 0.5 g, highlighting the pulley wireway system's greater resilience and reliability for installations in earthquake-prone areas.

Table 4
Test plan.

Step	Test	Direction	S_{DS} (g)	ZPA (g)	Scale factors (%)	Specimen under test	Tension (kgf)	Remark
1	1	X	0.2	–	–	Specimen 1	60	Resonance test
			0.2	–	–	Specimen 2	60	
	2	Y	0.2	–	–	Specimen 1	60	Resonance test
			0.2	–	–	Specimen 2	60	
	3	X, Y	0.5	0.6	100	Specimen 1	60	Design level excitation
			0.5	0.6	100	Specimen 2	60	
2	4	X	0.2	–	–	Specimen 1	60	Resonance test
			0.2	–	–	Specimen 2	60	
	5	Y	0.2	–	–	Specimen 1	60	Resonance test
			0.2	–	–	Specimen 2	60	
	6	X, Y	0.7	0.84	140	Specimen 1	60	Maximum considered
			0.7	0.84	140	Specimen 2	60	
3	7	X	0.2	–	–	Specimen 1	150	Resonance test
			0.2	–	–	Specimen 2	60	
	8	Y	0.2	–	–	Specimen 1	150	Resonance test
			0.2	–	–	Specimen 2	60	
	9	X, Y	0.5	0.6	100	Specimen 1	150	Design level excitation
			0.5	0.6	100	Specimen 2	60	
4	10	X	0.2	–	–	Specimen 1	150	Resonance test
			0.2	–	–	Specimen 2	60	
	11	Y	0.2	–	–	Specimen 1	150	Resonance test
			0.2	–	–	Specimen 2	60	
	12	X, Y	0.7	0.84	140	Specimen 1	150	Maximum considered
			0.7	0.84	140	Specimen 2	60	
5	13	X	0.2	–	–	Specimen 3	200	Resonance test
			0.2	–	–	Specimen 4	–	
	14	Y	0.2	–	–	Specimen 3	200	Resonance test
			0.2	–	–	Specimen 4	–	
	15	X, Y	0.5	0.60	100	Specimen 3	200	Design level excitation
			0.5	0.60	100	Specimen 4	–	

4.2. Dynamic properties results

4.2.1. Fundamental frequency results

Changes in natural frequency before and after testing are indicative of potential structural damage [29]. To detect such changes, resonance search tests were conducted before and after each main test, as detailed in Table 4. This method, combined with visual inspections, effectively identifies any damage sustained by the system.

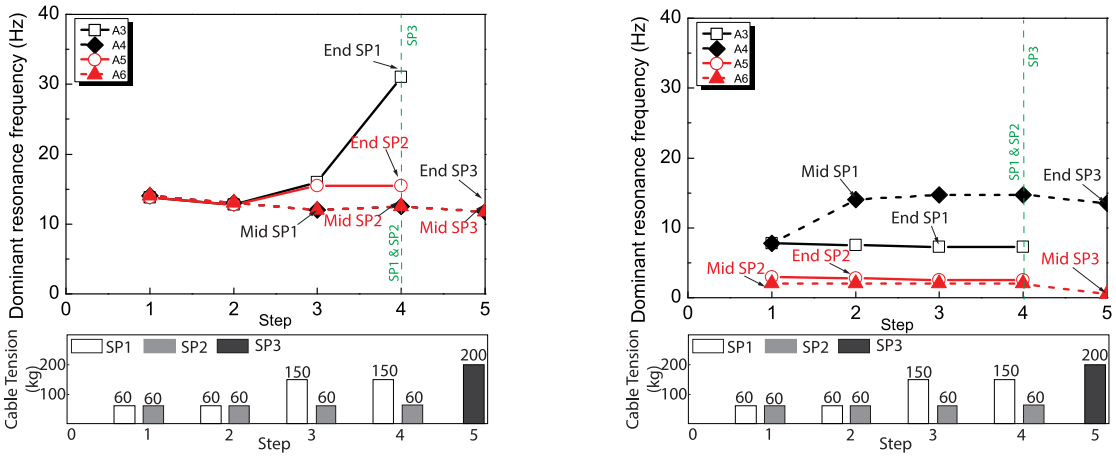
The tests were performed separately along the X and Y axes of the shaking table. Following FEMA 461 guidelines [30], a single-axis sinusoidal sweep covered a frequency range of 1.0 to 50 Hz at a rate of two octaves per minute. The fundamental frequencies of the specimens were identified using the frequency domain transfer function method [31], which relates the Fourier transform of the specimen acceleration data to that of the shaking table base. The transfer function was calculated using MATLAB's *tfestimate* function [32,33].

The fundamental frequencies (or dominant frequencies) of Specimens 1, 2, and 3 from Step 1 to Step 5 are shown in Fig. 9. The frequencies were measured at the end and midpoint positions, with values varying across steps and in both X and Y directions. The cable pretension values for each step and each specimen are also indicated. Specimens 1 and 2 were tested at Step 1 and Step 3 ($S_{DS} = 0.5$ g), and Step 2 and Step 4 ($S_{DS} = 0.7$ g). Specimen 3 was tested at Step 5 ($S_{DS} = 0.5$ g).

Based on Fig. 9, it is evident that Specimens 1 and 2 experienced increasing damage after successive earthquakes, with noticeable changes in fundamental frequency after each test step, particularly at the midpoint in the Y direction for Specimen 1 and at the end in the X direction for both Specimen 1 and Specimen 2. Additionally, suspended height (H), cable pretension, and hanger type affected the fundamental frequencies of the novel systems. The key findings are summarized as follows:

For Specimens 1 (Suspended height = 1000 mm) and 2 (Suspended height = 1800 mm) (Steps 1–4):

1. Step 1: Both specimens had nearly identical X direction frequencies at the midpoint and end. In the Y direction, the frequency at the ends was 7.75 Hz for both, while in the middle, Specimen 1 (3 Hz) was higher than Specimen 2 (2 Hz). Higher suspension height resulted in a lower Y direction frequency at the center.
2. Steps 1-2: Both specimens showed similar frequency changes, except Specimen 1 (1000 mm) had an 80.64% increase at the midpoint in the Y direction, indicating earlier damage due to lower suspension height.
3. Steps 2-3: Slight changes in X and Y frequencies at the midpoint and end were observed. Both specimens showed a 16.36% increase in fundamental frequency, indicating progressive damage, primarily at the end in the X direction. Increasing cable tension from 60 kgf to 150 kgf had limited effect at design-level excitation.



(a) X direction. (b) Y direction.

Fig. 9. The dominant frequencies of the Specimens 1 and 2 from steps 1–4 (A3 - End of SP1; A5 - End of SP2; A4 - Middle of SP1; and A6 - Middle of SP2); Specimen 3 at step 5 (End - Middle of SP3; and A6 - Middle of SP3.

4. Step 3-4: Similar frequency trends to Step 2–3, with a significant 2.25 times increase at the end of Specimen 1, indicating continued damage accumulation. Higher tension (150 kgf) caused significant end damage under high-intensity seismic excitation.

For Specimens 2 (with main hangers) and 3 (without main hangers):

1. Specimen 3 had 16.07% lower X direction frequency and 75% lower Y direction frequency at the midpoint compared to Specimen 2.
2. At the end, Specimen 3 had 24.19% lower X direction frequency and 350% higher Y direction frequency compared to Specimen 2.
3. Main hangers enhance the stiffness of the pulley wireway system, particularly in the Y-axis direction.

4.2.2. *Damping ratio results*

The damping ratio's variation is a critical indicator of structural damage, closely correlating with shifts in fundamental frequency and the damage observed at each step of testing. The damping ratios ζ were calculated after each test step at the fundamental frequency using the half-power bandwidth method, as detailed below [34–36]:

$$\zeta = \frac{f_2 - f_1}{2f_0} \times 100\% \tag{7}$$

where:

- f_0 is the frequency at the peak of the transfer function amplitude.
- f_1 and f_2 are the frequencies at which the amplitude drops to $\frac{1}{\sqrt{2}}$ of the peak transfer function amplitude on either side of f_0.

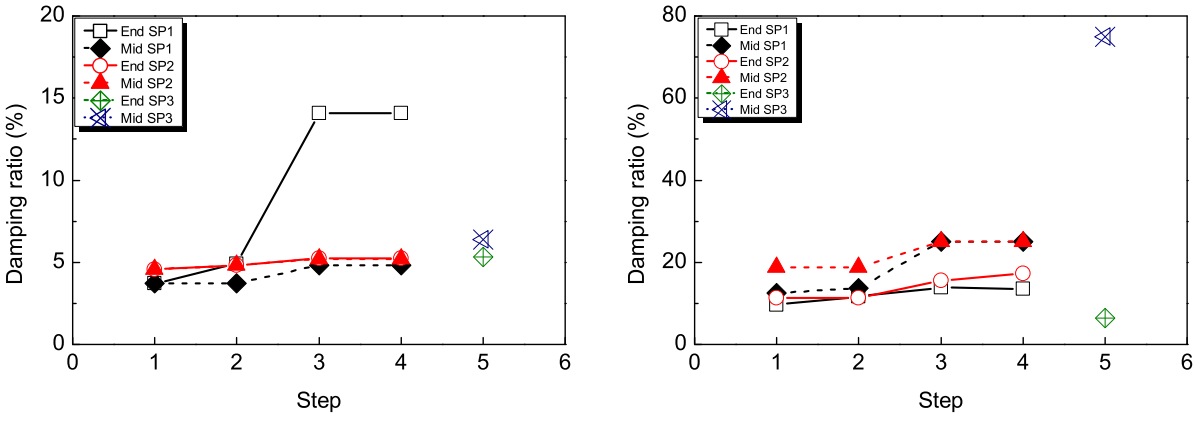
As shown in Fig. 10, the initial damping ratio at Step 1 for Specimens 1, 2, and 3 varied between 3.7% and 6.4% in the X direction, and between 9.96% and 75% in the Y direction. It is evident that the damping ratio is influenced by the support configuration of the specimens. Specifically, for Specimens 1 and 2, which had full support with main hangers, connectors, and sub-hangers, the higher suspension height in Specimen 2 resulted in a greater damping ratio. In contrast, the absence of main hangers in Specimen 3 led to a significant increase in the damping ratio, particularly at the midpoint of the specimen in the Y direction.

To assess the changes in the system's damping behavior during testing, the Damping ratio increase factor (DRIF) is introduced, as shown in Fig. 11. The DRIF quantifies the relative change in damping ratio at each subsequent step compared to the initial step (Step 1). It is calculated as:

$$\text{DRIF} = \frac{\zeta_n}{\zeta_1} \tag{8}$$

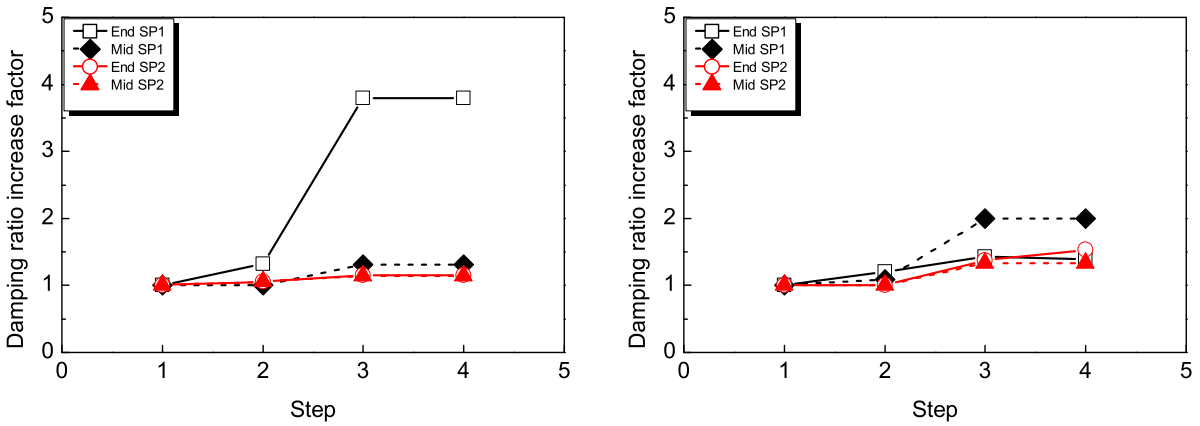
where ζ_n represents the damping ratio at step n, and ζ_1 is the damping ratio at the initial step.

In Specimen 2, with a constant cable pretension of 60 kgf throughout Steps 1 to 4, DRIF values steadily increased from 1 to 1.15 in the X direction and from 1 to 1.53 in the Y direction, reflecting progressive damage accumulation and consistent with earlier frequency shifts.



(a) X direction. (b) Y direction.

Fig. 10. Variation of damping ratio of test specimens at different locations.



(a) X direction. (b) Y direction.

Fig. 11. Damping ratio increase factor (DRIF) of test specimens 1 and 2.

Specimen 1, under the same 60 kgf pretension during Steps 1 and 2, started with similar DRIF values in Step 1 but showed slightly higher DRIFs than Specimen 2 in both X and Y directions, particularly at the end and mid-span. This suggests that the lower suspension height of Specimen 1 led to greater damage, correlating with observed frequency variations.

When the cable pretension in Specimen 1 increased to 150 kgf during Steps 3 and 4, DRIF values rose sharply, reaching 3.8 in the X direction at the end and 2.0 in the Y direction at the mid-span. This significant rise, with no substantial additional damage between Steps 3 and 4 compared to Steps 1 and 2, indicates that higher cable pretension enhances the system's damping capacity.

4.3. Displacement response

The static LVDT data were calibrated to determine the relative displacement response of the test specimen, calculated using:

$$r_x = x - x_o \tag{9a}$$

$$r_y = y - y_o \tag{9b}$$

where r_x and r_y are the relative displacements in the X and Y directions, respectively. x_o and y_o are the absolute displacements from the base of the shaking table, while x and y are from specified locations on the specimens and test frame. The relative displacement response-time histories at the center and end of three pulley wireway system specimens are shown in Fig. 12.

Fig. 13 shows the maximum relative displacement response of the test specimen and ceiling of the test frame at various experimental steps. The ceiling displayed consistent maximum relative displacement for equivalent earthquake magnitudes. Specifically, the maximum displacement was 4.3 mm (X) and 11.72 mm (Y) in step 1 and step 3, and 6.64 mm (X) and 15.78 mm (Y) in step 2 and step 4. The steel frame demonstrated satisfactory stiffness, meeting the specified requirements.

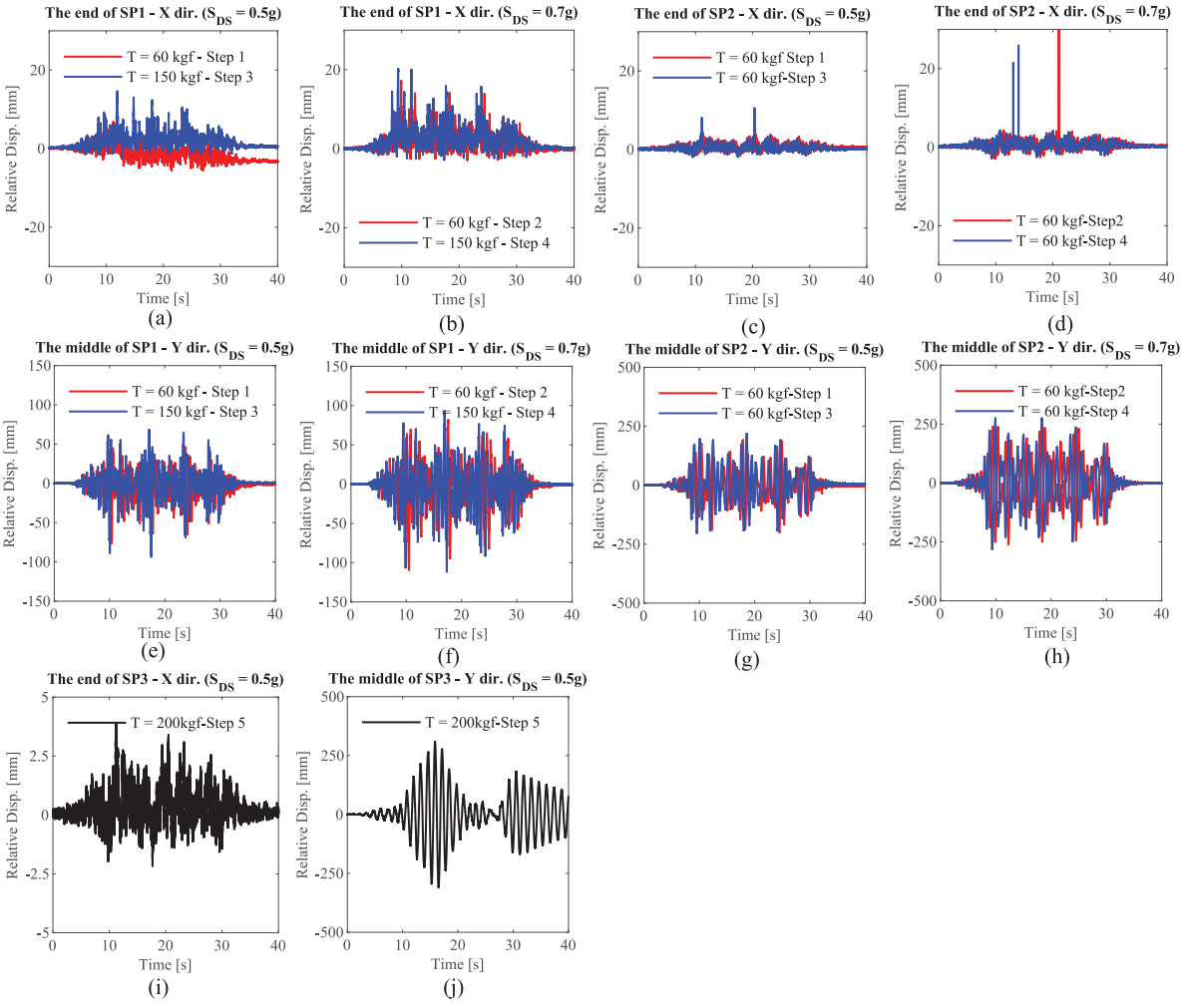
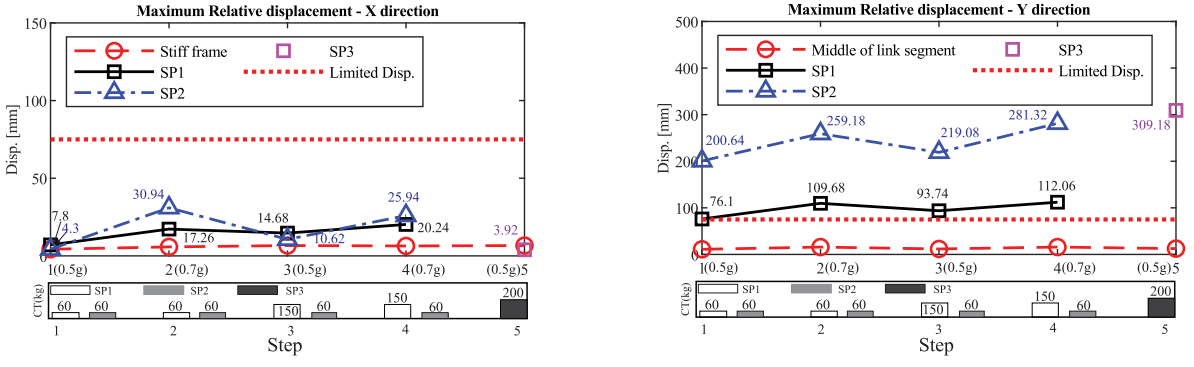


Fig. 12. Relative displacement response-time history results.



(a) X-direction. (b) Y-direction.

Fig. 13. Maximum relative displacement response results.

Furthermore, in accordance with the guidelines and suggestions put forth by the Korean National Radio Research Agency [37], it is essential that the displacement at the top of the equipment should not surpass 75 mm in order to guarantee the secure and efficient functioning of non-structural elements, as well as neighboring components. The figure shows that. Throughout all experimental steps, it was observed that the maximum relative displacements of Specimens 2 and 3 in the Y-direction exceeded the boundary limit of 75 mm. The maximum relative displacements of Specimen 1 in the Y-directions were found to meet the requirements during step 1. However, in subsequent experimental steps (i.e., steps 3), this value exceeded the suggested boundary limit of 25%.

Based on Fig. 12 and Fig. 13, it is evident that Specimens 1 and 2 experienced increasing damage after successive earthquakes, with relative displacements in later steps being larger than in earlier steps under the same earthquake magnitude. For example, the maximum relative displacement of Specimen 2 in the Y direction was 9.19% higher in step 3 than in step 1 (S_{DS} = 0.5 g), and 8.54% higher in step 4 than in step 2 ((S_{DS} = 0.7 g). Additionally, the suspended height (H), cable pretension, and hanger type affected the relative displacement responses. The key findings are summarized as follows:

1. Effect of suspended height on the relative displacement response:
   (a) Specimen 1 (H = 1000 mm) had an 81.39% higher maximum relative displacement in the X direction (S_{DS} = 0.5 g – Step 1) and a 131.40% reduction in the same direction (S_{DS} = 0.7 g – Step 2) compared to Specimen 2 (H = 1800 mm).
   (b) At the 100% design level (S_{DS} = 0.5 g - Step 1), Specimen 1 exhibited 163.65% lower maximum relative displacement in the Y direction, and further decreased to 136.30% lower at S_{DS} = 0.7 g – Step 2, compared to Specimen 2.
   (c) Overall, these findings suggest that reducing the suspended height can effectively reduce displacement responses.
2. Effect of pre-tension of the cables on the relative displacement response:
   (a) Overall, increasing cable tension stabilizes the displacement of the system in the X and Y direction. Specifically, the maximum relative displacement increased by 121.28% and 44% from Step 1 (S_{DS} = 0.5 g) to Step 2 (S_{DS} = 0.7 g) at T = 60 kg. However, when T = 150 kg, the maximum relative displacement increased by only 37.87% and 19.5% from Step 3 (S_{DS} = 0.5 g) to Step 4 (S_{DS} = 0.7 g).
3. Effect of support configurations on the relative displacement response:
   (a) Specimen 2 (Step 1) with main hangers showed 54.09% lower relative displacement in the Y direction compared to Specimen 3 (Step 5) without main hangers, while in the X direction, the relative displacements of both specimens were similar. This suggests that using main hangers significantly reduces the displacement of the novel system during earthquakes.

4.4. Evaluating the seismic response of the specimens

A thorough examination in the frequency domain was conducted to investigate the seismic response of the specimens under artificial earthquakes. The dynamic response was estimated using time-domain measurements from accelerometers (A3, A4, A5, and A6) located at the end and midpoint of the specimens, then transformed into the frequency domain. The acceleration spectral density (ASD) and acceleration root mean square (ARMS) functions were used to evaluate and compare the dynamic behavior of the pulley wireway system and an existing system specimen.

The ASD plot depicts the acceleration response distribution for each frequency measured using the shaking table experiment. An approach for calculating the ASD functions of the measured data is Welch's method [38,39]. Denote the mth windowed, zero-padded frame from the signal x as follows:

$$x_m(n) \triangleq \omega(n)\, x(n + mR) \tag{10}$$

$n = 0, 1, \ldots, M-1, m = 0, 1, \ldots, K-1$ where R is defined as the window hop size and let K denote the number of available frames. Then, the periodogram of the mth block is given by:

$$P_{x_m,M}(\omega_k) = \frac{1}{M}\left|\mathrm{FFT}_{N,k}(x_m)\right|^2 \triangleq \frac{1}{M}\left|\sum_{n=0}^{N-1} x_m(n)\, e^{-j2\pi nk/N}\right|^2 \tag{11}$$

As previously noted, the Welch estimate of the power spectral density is as follows:

$$\hat{S}_x^w(\omega_k) \triangleq \frac{1}{K}\sum_{m=0}^{K-1} P_{x_m,M}(\omega_k) \tag{12}$$

In this study, three pulley wireway system specimens were dynamic analyzed to assess the seismic performance of the system with varying suspension height, cable pre-tension force, and hangers based on the data from the measurement devices. The ASD was calculated using Welch's approach on the basis of acceleration response records for end and middle position of three different specimens of pulley wireway system subjected to 100% and 140% AC156 input motion.

Fig. 14 depict ASD plots of Specimens 1, 2 and 3 in the X, and Y directions, respectively. Acceleration spectra were calculated using the pwelch function in MATLAB. The ASD values are displayed between 1 and 256 Hz. The following parameters were used to calculate ASD in this study: M = 1024 points per segment, K = 21, segments with 50% duplicates S = 0.5M, time per segment = 2 s, and df = 0.5 Hz are utilized as input parameters for the ASD calculation.

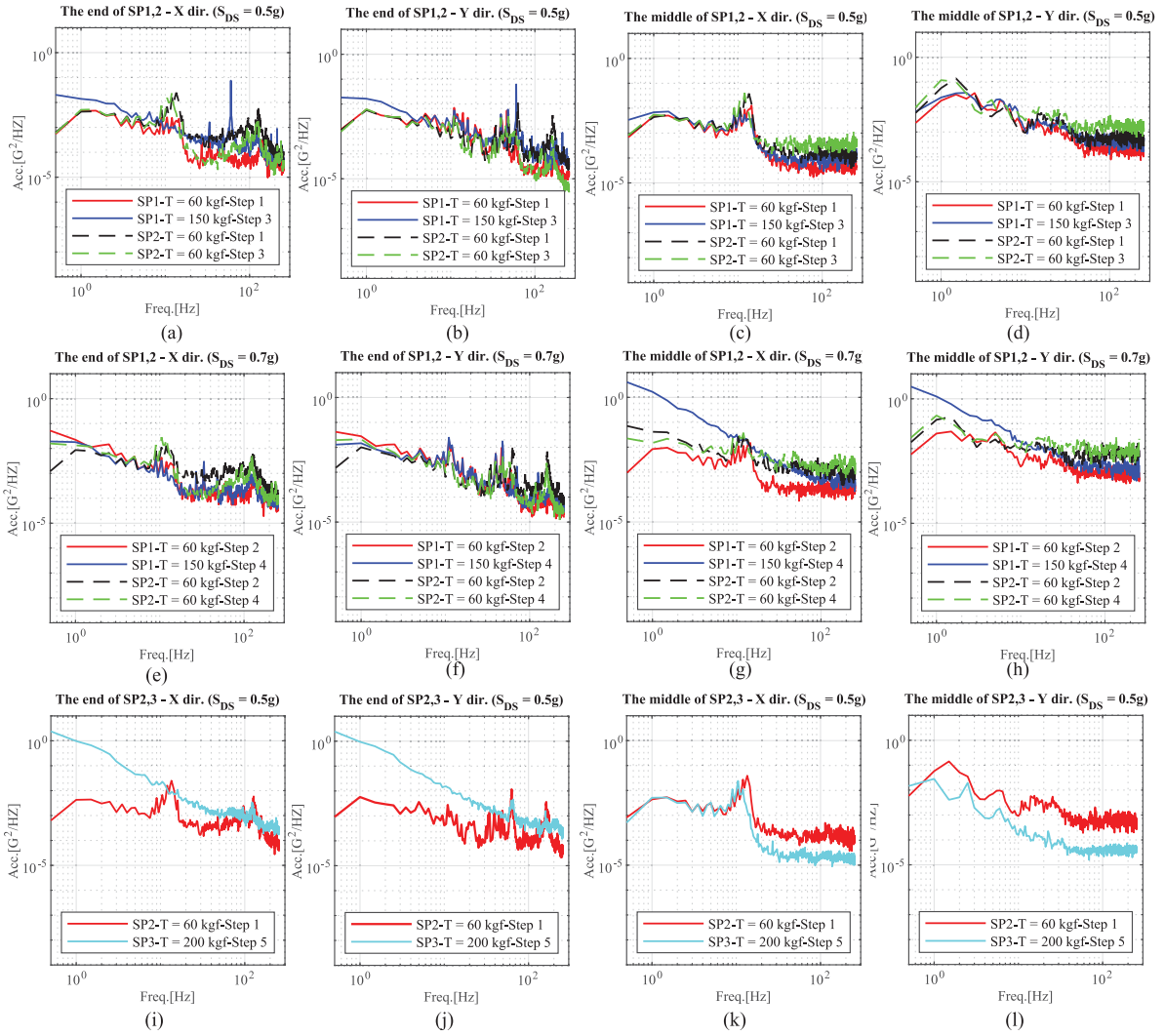


Fig. 14. The acceleration spectral density (ASD) plots of Specimens 1,2 and 3.

Table 5
The maximum ASD values of the Specimens 1, 2 and 3.

Direction	Step	Peak ASD (G^2/Hz) vs Frequency (Hz)											
		End SP1		Mid SP1		End SP2		Mid SP2		End SP3		Mid SP3	
		ASD	Freq.	ASD	Freq.	ASD	Freq.	ASD	Freq.	ASD	Freq.	ASD	Freq.
X	1	0.005	1.50	0.013	14.50	0.025	13.50	0.039	13.50	–	–	–	–
	2	0.052	0.50	0.015	14.50	0.013	12.00	0.071	0.50	–	–	–	–
	3	0.075	60.00	0.008	10.50	0.026	12.00	0.041	12.00	–	–	–	–
	4	0.019	0.50	4.067	0.50	0.028	10.50	0.038	12.00	–	–	–	–
	5	–	–	–	–	–	–	–	–	2.397	0.50	0.024	10.50
Y	1	0.007	11.00	0.037	2.50	0.012	63.00	0.142	1.50	–	–	–	–
	2	0.042	0.50	0.048	1.50	0.013	63.50	0.189	1.50	–	–	–	–
	3	0.062	60.00	0.038	2.00	0.006	1.00	0.120	1.00	–	–	–	–
	4	0.024	11.00	3.065	0.50	0.019	0.50	0.212	1.00	–	–	–	–
	5	–	–	–	–	–	–	–	–	2.437	0.50	0.028	1.00

4.4.1. Effect of suspended height

The investigation aimed to determine the impact of suspended height on the seismic responses of the novel systems. The peak ASD values with corresponding frequencies of the three specimens at Steps 1 to 5 are shown in Table 5

Based on frequency domain analysis of Specimens 1 and 2 subjected to simulated earthquakes, an analysis was conducted on the impact of suspended height (H) on seismic responses at two different intensities, S_{DS} = 0.5 g and 0.7 g (see Fig. 14(a–h) and Table 5). The findings are summarized as follows:

1. Step 1 (S_{DS} = 0.5 g):
   (a) End of Specimen – X direction:
      i. Below 3 Hz: Both Specimen 1 (H=1000 mm) and Specimen 2 (H = 1800 mm) exhibited similar ASD spectra, indicating that H has negligible effects on seismic response within this frequency range.
      ii. Above 3 Hz: Specimen 1 consistently registered lower ASD than Specimen 2, with a peak ASD reduction of five times, suggesting that decreased seismic responses are associated with smaller H.
   (b) End of Specimen – Y direction:
      i. Below 3 Hz: ASD results paralleled those in the X direction, confirming minimal impact of H.
      ii. Above 3 Hz: Specimen 1 displayed higher ASD from 3–30 Hz but lower values beyond 30 Hz, with a peak ASD reduction of 1.71 times compared to Specimen 2.
   (c) Mid of Specimen – X and Y directions:
      i. Below 3 Hz: ASDs were comparable, reinforcing the minimal impact of H.
      ii. Above 3 Hz: Specimen 1 consistently showed lower ASD than Specimen 2, with peak reductions of 3.00 times in the X direction and 3.84 times in the Y direction, highlighting reduced seismic responses due to lower H.
2. Step 2 (S_{DS} = 0.7 g):
   (a) End of Specimen – X direction:
      i. Below 3 Hz: Specimen 1 exhibited higher ASD, indicating stronger seismic responses at lower H. The peak ASD of Specimen 1 was more than four times that of Specimen 2.
      ii. Above 3 Hz: Specimen 1 consistently showed lower ASD than Specimen 2, indicating that smaller H reduces the seismic response of novel systems in this frequency range.
   (b) End of Specimen – Y direction:
      i. Below 30 Hz: Higher ASD was observed for Specimen 1.
      ii. Above 30 Hz: Lower ASD values were recorded.
      iii. Peak ASD: The peak ASD of Specimen 1 was 3.23 times higher, demonstrating a significant escalation in response with increased seismic intensity.
   (c) Mid of Specimen – X and Y directions:
      i. Across all frequencies, Specimen 1 maintained lower ASD than Specimen 2, with peak ASDs 4.73 times and 3.94 times lower in the X and Y directions, respectively, affirming lower seismic responses at reduced heights.
3. A marked alteration in the ASD spectrum was observed when the intensity increased from 0.5 g to 0.7 g, particularly below 3 Hz. This shift revealed a sharp increase in the seismic response of lower H systems, while those with higher H showed minimal variation in ASD distribution. This finding indicates that systems with lower structural heights are more sensitive to increases in seismic intensity.

These analyses demonstrate that systems with lower suspended heights generally exhibited lower seismic responses but increased sensitivity to seismic activities, particularly at lower frequencies and higher earthquake intensities. This suggests that suspended height plays an important role in dynamic behavior of the novel systems during earthquakes.

4.4.2. Effect of cable pre-tension

Based on frequency domain analysis of Specimen 1 subjected to simulated earthquakes, an analysis was conducted on the impact of cable pre-tension (T) on seismic responses at two different intensities, S_{DS} = 0.5 g and 0.7 g (see Fig. 14(a–h) and Table 5). The findings are summarized as follows:

1. For Step 1 (T = 60 kgf) and Step 3 (T = 150 kgf) at S_{DS} = 0.5 g:
   (a) End of Specimen – X direction:
      • Across all frequencies, Specimen 1 with T = 60 kgf consistently exhibited lower ASD compared to when T = 150 kgf. The peak ASD was 15 times lower at T = 60 kgf, indicating that higher tension significantly increases seismic response.

(b) End of Specimen – Y direction:

- Similarly, Specimen 1 with $T = 60$ kgf consistently displayed lower ASD across all frequencies, with a peak ASD 8.8 times lower than at $T = 150$ kgf, suggesting a significant increase in seismic response at higher tensions.

(c) Mid of Specimen – X direction:

- Although generally lower ASD was observed for $T = 60$ kgf across all frequencies, the peak ASD was 1.60 times higher than at $T = 150$ kgf.

(d) Mid of Specimen – Y direction:

- ASD values were consistently lower for $T = 60$ kgf across all frequencies, with peak ASD equivalent to that at $T = 150$ kgf.

2. For Step 2 ($S_{DS} = 0.7$ g):

(a) End of Specimen – X direction:

- Specimen 1 with $T = 60$ kgf showed higher ASD compared to $T = 150$ kgf in the 0–30 Hz frequency range, with the peak ASD 2.74 times higher, demonstrating that higher tension stabilizes seismic response in this direction.

(b) End of Specimen – Y direction:

- Higher ASD was consistently observed for $T = 60$ kgf across all frequencies, with the peak ASD 1.75 times higher, indicating a stabilizing effect of higher tension on seismic responses.

(c) Mid of Specimen – X direction:

- Significant lower ASD was noted for $T = 60$ kgf across all frequencies, with the peak ASD 271.13 times lower, suggesting that higher tension leads to an increased anomaly in seismic response.

(d) Mid of Specimen – Y direction:

- Consistently lower ASD was observed for $T = 60$ kgf, with the peak ASD 63.85 times lower, indicating increased anomalies in seismic responses at higher tensions.

This finding highlights the critical role of cable tension in modulating the dynamic response of structural systems under seismic loading. Higher tensions tend to stabilize responses under low earthquake intensities but may exacerbate responses, especially at the midpoint, under high earthquake intensities.

4.4.3. Effect of support configurations

Based on frequency domain analysis of Specimen 2, equipped with both sub and main hangers, and Specimen 3, used only with sub-hangers, both subjected to a simulated earthquake, an analysis was conducted on the impact of hanger types on seismic responses at an earthquake intensity of $S_{DS} = 0.5$ g (see Fig. 14(i–l) and Table 5). The findings are summarized as follows:

In an analysis comparing Specimen 2 (Step 1 -$T = 60$ kgf) and Specimen 3 (Step 5 -$T = 200$ kgf) at $S_{DS} = 0.5$ g:

1. End of Specimen – X direction:

(a) Across the entire frequency range, Specimen 2 consistently exhibited ASD than Specimen 3, especially in the low frequency range, where the peak ASD of Specimen 2 was 95.88 times lower than that of Specimen 3. This suggests that higher tensions significantly increase the seismic response in the X direction when main hangers are absent.

2. End of Specimen – Y direction:

(a) Similarly, Specimen 2 consistently showed lower ASD across all frequencies, with the peak ASD being 203.08 times lower than that of Specimen 3, indicating a significant increase in seismic response in the Y direction due to higher tensions in the absence of main hangers.

3. Mid of Specimen – X direction:

(a) From 0-30 Hz, Specimen 2 displayed a similar ASD spectrum to Specimen 3.
(b) Above 30 Hz, Specimen 2 consistently had higher ASD, with the peak ASD 1.63 times greater than Specimen 3, suggesting reduced X-direction stiffness at the mid-position reduces seismic response when lacking main hangers.

4. Mid of Specimen – Y direction:

(a) Throughout all frequencies, Specimen 2 consistently showed higher ASD than Specimen 3, with the peak ASD being 5.07 times greater, indicating decreased Y-direction stiffness at the mid-position exacerbates seismic response when main hangers are absent.

This finding illustrates the influence of support configurations on seismic responses. The absence of main hangers, combined with increased cable tension, reduces response at the midpoint but introduces instability at the end. Elevated cable tensions exacerbate responses, especially without main hangers.

4.4.4. Effect of the fundamental frequencies

This section examines how variations in the fundamental frequency of Specimen 2 impact its ASD. The TRS of the input acceleration is frequency-dependent, peaking between 1 to 10 Hz in the X direction and 1 to 9 Hz in the Y direction, as shown in Fig. 8. Frequencies outside these ranges experience decreased TRS values, indicating that shifts in Specimen 2's fundamental frequencies significantly influence its spectral accelerations.

Fig. 14(a-h) and Fig. 9 illustrate that, at the end position, as the fundamental frequency in the X direction increased from 13.75 Hz to 15.5 Hz between Steps 1 and 3 ($S_{DS} = 0.5$ g), ASD values decreased because these frequencies moved beyond the TRS peak range. A similar trend was observed from Steps 2 to 4 ($S_{DS} = 0.7$ g), with a frequency increase from 12.75 Hz to 15.5 Hz leading to further ASD reduction.

In contrast, at the middle position, the fundamental frequency in the X direction decreased from 14 Hz to 12 Hz between Steps 1 and 3 ($S_{DS} = 0.5$ g), resulting in an increase in ASD. This trend continued from Steps 2 to 4 ($S_{DS} = 0.7$ g), with a further frequency drop from 13 Hz to 12.5 Hz, causing a corresponding rise in ASD.

4.5. Evaluating the earthquake energy of the specimens

The root mean square acceleration (ARMS) is a measure of the energy accumulated in a structure as a result of an earthquake. The term "ARMS" refers to the root mean square of the square of the acceleration response during a certain time period (sampling time), which may be computed using Eq. (13) [40]. Here, a(t) denotes the time-dependent acceleration response; t_0 denotes the start time; T_d denotes the vibration measurement time, and $E(T_D)$ denotes the total energy for the period T_d.

$$RMS_a = \frac{E(T_d)}{T_d} = \left[\frac{1}{T_d}\int_{t_0}^{t_o+T_d} a^2(\tau)d\tau\right]^{1/2} \tag{13}$$

Similarly, temporal RMS can be defined by replacing T_d with a small-time interval Δt as follows:

$$RMS_a(t) = \left[\frac{1}{\Delta t}\int_{t}^{t+\Delta t} a^2(\tau)d\tau\right]^{1/2} \tag{14}$$

for $\Delta t \to 0$

In the frequency domain, the ARMS is defined as the square root of the area under the ASD curve. The area under the ASD curve of the jth frequency segment (a_j) between the frequencies f_{i-1} and f_i corresponds to P_{i-1} and P_i [41].

m is the slope of the segment j between the frequencies f_{i-1} and f_i:

$$m = 10\log\left(\frac{P_i}{P_{i-1}}\right)\frac{\log(2)}{\log\left(\frac{f_i}{f_{i-1}}\right)} \tag{15}$$

for $m \neq -10\log(2)$:

$$a_{f_i,j} = 10\log(2)\frac{P_i}{10\log(2)+m}\left[f_i - f_{i-1}\left(\frac{f_{i-1}}{f_i}\right)^{m/10\log(2)}\right] \tag{16}$$

for $m = -10\log(2)$:

$$a_{f_i,j} = P_{i-1}f_{i-1}\ln\left(\frac{f_i}{f_{i-1}}\right) \tag{17}$$

The GRMS value at jth frequency segment:

$$ARMS_j = \sqrt{a_j} \tag{18}$$

The overall RMS level at jth at frequency f_i is then:

$$ARMS_{f_i} = \sum_{m=0}^{j} a_m \tag{19}$$

The ARMS value was used to measure the seismic energy of a system. In the frequency domain, the ARMS values of the vibration response are determined using cumulative distribution functions (CDF). The CDF curves are depicted in Fig. 15 correspond to the X, and Y directions for three pulley wireway system specimens subjected to a 100% and 140% AC156 input motion. The overall ARMS is the value at the end of the CDF curves, as shown in Fig. 16

In this study, three pulley wireway system specimens were dynamically analyzed to assess their seismic performance, varying suspension height, cable pre-tension force, and hanger types. The findings demonstrate that suspended height (H), cable pretension, and hanger type significantly influence the seismic performance of these novel systems. Key findings are summarized in this section.

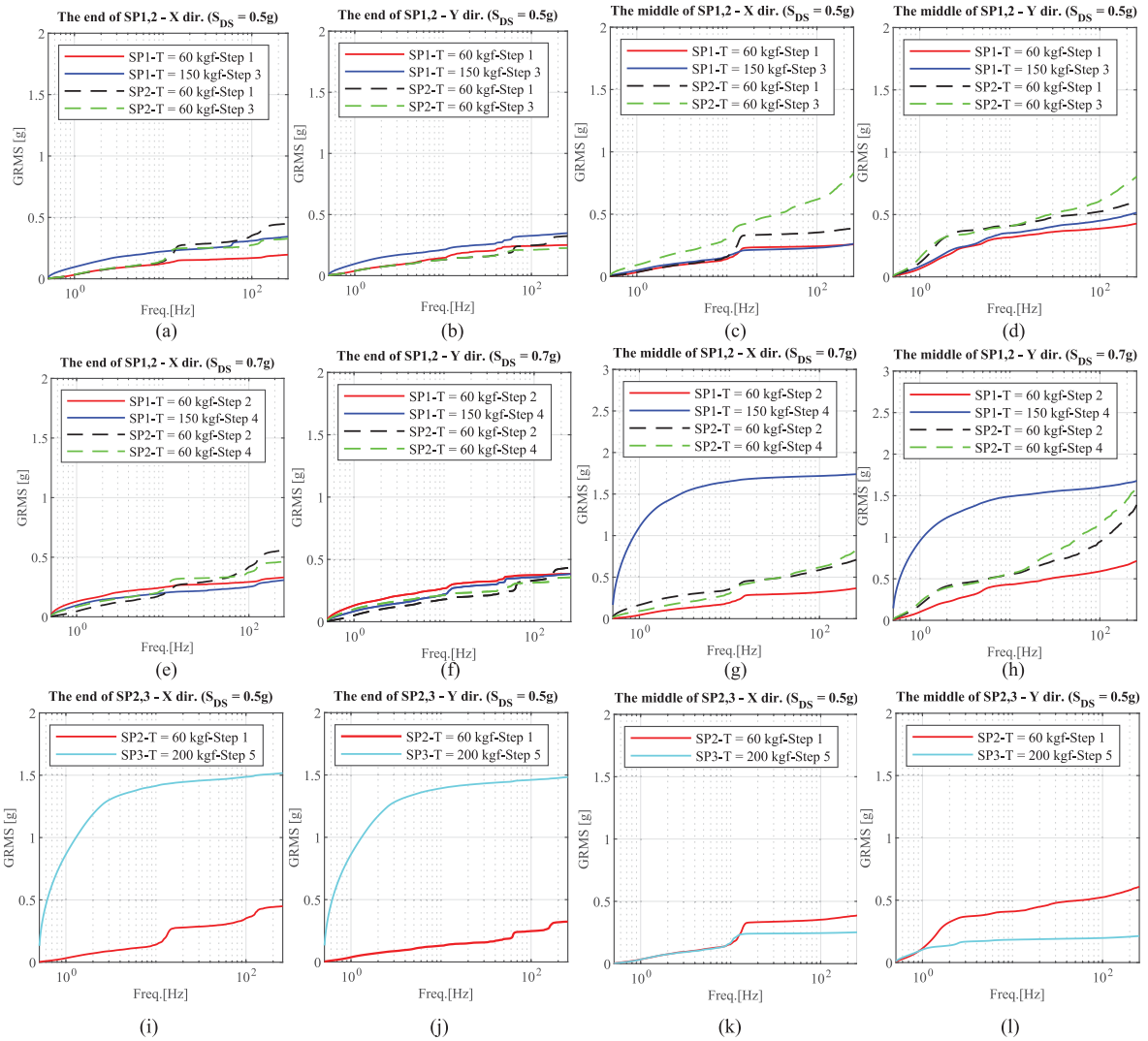


Fig. 15. Cumulative acceleration root mean square plots (CDF curves) of Specimens 1, 2 and 3.

4.5.1. Effect of suspend height

Based on frequency domain analysis of Specimens 1 and 2 subjected to simulated earthquakes, an analysis was conducted on the impact of H on seismic energy at two different intensities, S_{DS} = 0.5 g and 0.7 g (see Fig. 15(a–h) and Fig. 16(a–d)). The findings are summarized as follows:

1. Step 1 (T = 60 kgf, S_{DS} = 0.5 g):

   (a) End of Specimen – X Direction:

      i. From 0 to 10 Hz, the CDF curves for Specimen 1 (H = 1000 mm) and Specimen 2 (H = 2000 mm) were nearly identical.

      ii. Above 10 Hz, Specimen 1 exhibited stable seismic energy across all frequencies, while Specimen 2 showed a sudden increase in seismic energy around its first and second mode frequencies. The overall ARMS for Specimen 2 was 2.28 times that of Specimen 1, suggesting increased seismic energy due to heightened structural resonance.

   (b) End of Specimen – Y Direction:

      i. Similar patterns as in the X direction were observed, but above 10 Hz, Specimen 2 showed reduced seismic energy from 10-70 Hz followed by a sudden increase around its second and third mode frequencies. Its overall ARMS was 1.29 times that of Specimen 1, reflecting resonance effects due to increased height.

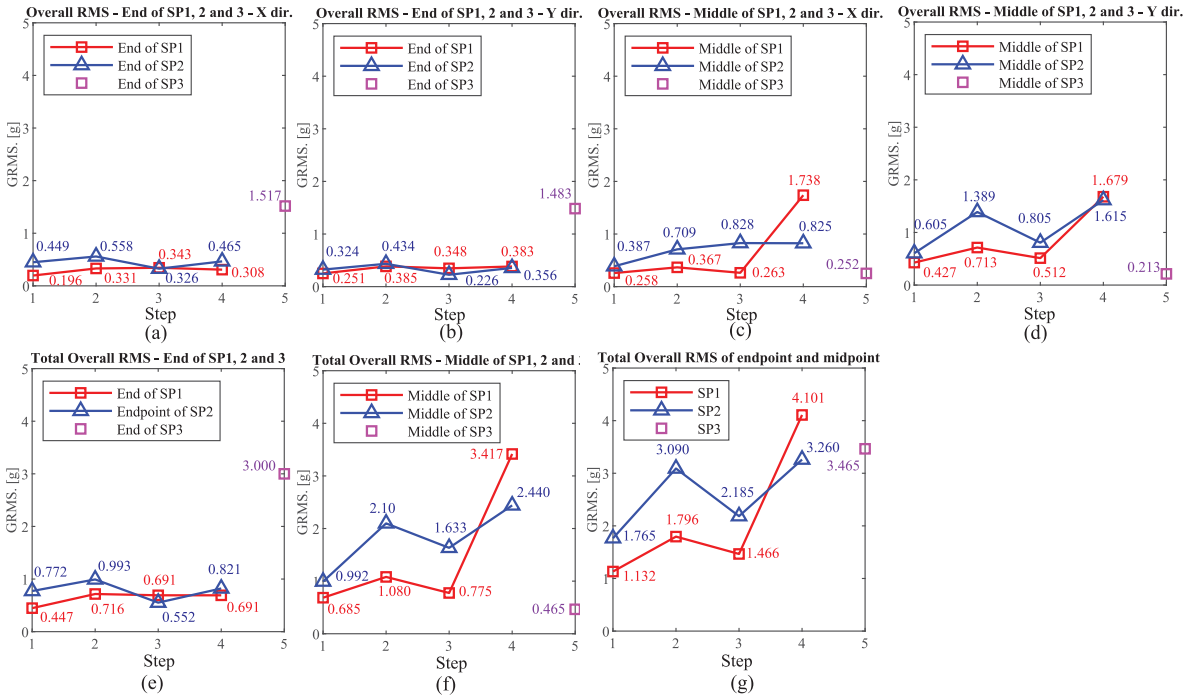


Fig. 16. Overall ARMS of acceleration response of the Specimens 1,2 and 3.

(c) Mid of Specimen – X and Y Directions:

i. Across all frequencies, the CDF curves of Specimen 1 were consistently lower than those of Specimen 2.
ii. Near the natural oscillation frequencies (10-20 Hz for X and 1-3 Hz for Y), both specimens experienced a sudden increase, with Specimen 2 showing a more substantial rise. The overall ARMS of Specimen 2 was significantly higher, at 1.49 in the X direction and 1.42 in the Y direction, indicating increased seismic energy from higher structural heights.

2. Step 2 (T = 60 kgf, S_{DS} = 0.7 g):

(a) End of Specimen – X Direction:

i. From 0 to 10 Hz, the seismic energy of Specimen 1 (H = 1000 mm) was greater than that of Specimen 2 (H = 2000 mm).
ii. Above 10 Hz, while Specimen 1 maintained consistent seismic energy across all frequencies, Specimen 2, with a suspension height 1.8 times greater than Specimen 1, exhibited a sudden increase in seismic energy around its first and second mode frequencies. The overall ARMS for Specimen 2 was 1.69 times that of Specimen 1.

(b) End of Specimen – Y Direction:

i. From 0 to 60 Hz, the seismic energy of Specimen 1 was greater than that of Specimen 2.
ii. Above 60 Hz, while Specimen 1 maintained consistent seismic energy, Specimen 2 began showing a sudden increase around its second and third mode frequencies. The overall ARMS for Specimen 2 was 1.12 times that of Specimen 1.

(c) Mid of Specimen – X and Y Directions:

i. The CDF curve of Specimen 1 consistently showed lower values across all frequencies compared to Specimen 2.
ii. Near the natural frequencies of 10-20 Hz for X and 1-3 Hz for Y, both specimens showed a significant increase in CDF values, with Specimen 2 exhibiting a larger increase. The overall ARMS of Specimen 2 was considerably higher, at 1.93 in the X direction and 1.94 in the Y direction, indicating increased seismic energy from the greater height.

For S_{DS} = 0.5 g: Based on Fig. 16 (e-g), increasing the suspension height from 1000 mm to 1800 mm resulted in an increase in seismic energy across the system, with seismic energy increasing by 1.73 times at the end positions, 1.45 times at the mid positions, and an average increase of 1.56 times across both mid and end positions.

For $S_{DS} = 0.7$ g: Similarly, raising the suspension height from 1000 mm to 1800 mm led to enhanced seismic responses, marked by a 1.38 times increase at the end positions, a 1.91 times increase at the mid positions, and an overall average increase of 1.72 times across the system (see Fig. 16(e-g)).

These findings highlight the critical influence of suspension height on seismic energy within structural systems, demonstrating that structures with larger suspension heights tend to amplify seismic responses, particularly at increased seismic intensities. This underscores the importance of considering suspension height in the seismic design of novel systems.

4.5.2. Effect of cable pre-tension

In the investigation of seismic responses under different spectral acceleration levels ($S_{DS} = 0.5$ g and $S_{DS} = 0.7$ g), the behavior of Specimens 1 (maintaining tension T at 60 kgf from Step 1 to Step 2, and at 150 kgf from Step 3 to Step 4) and Specimen 2 (maintaining tension T at 60 kgf from Step 1 to Step 4) was analyzed. Based on Fig. 15 (a–h) and Fig. 16(a–d)The findings were as follows:

1. Specimen 2 with $T = 60$ kgf from Step 1 to Step 4
   (a) Steps 1 and Step 3 ($S_{DS} = 0.5$ g)
      i. End of Specimen – X Direction: The CDF curve at Step 3 was lower than at Step 1 for frequencies above 10 Hz. The overall ARMS at Step 1 was approximately 1.38 times higher than at Step 3 due to cumulative damage.
      ii. End of Specimen – Y Direction: The CDF curve at Step 3 was lower than at Step 1 for frequencies above 60 Hz. The overall ARMS at Step 2 was about 1.43 times higher than at Step 3.
      iii. Mid of Specimen – X Direction: The CDF curve at Step 3 was higher than at Step 1 for frequencies above 10 Hz. The overall ARMS at Step 1 was approximately 2.10 times higher than at Step 3.
      iv. Mid of Specimen – Y Direction: The CDF curve at Step 3 was higher than at Step 1 for frequencies above 10 Hz. The overall ARMS at Step 1 was about 1.32 times higher than at Step 3.
   (b) Steps 2 and Step 4 ($S_{DS} = 0.7$ g)
      i. End of Specimen – X Direction: The overall ARMS at Step 2 was approximately 1.20 times higher than at Step 4 due to cumulative damage.
      ii. End of Specimen – Y Direction: The overall ARMS at Step 2 was about 1.22 times higher than at Step 4.
      iii. Mid of Specimen – X Direction: The overall ARMS at Step 4 was approximately 1.16 times higher than at Step 2.
      iv. Mid of Specimen – Y Direction: The overall ARMS at Step 4 was about 1.16 times higher than at Step 2.
   (c) For Specimen 2: Cumulative damage from successive earthquakes led to a decrease in seismic energy at the end and an increase at the mid positions. Based on Fig. 14(e–g) For $S_{DS} = 0.5$ g, damage resulted in a 1.39 times decrease in seismic energy at the end and a 1.65 times increase at the mid. For $S_{DS} = 0.7$ g, there was a 1.20 times decrease at the end and a 1.16 times increase at the mid.
2. Specimen 1 with $T = 60$ kgf from Step 1 to Step 2 and $T = 150$ kgf from Step 3 to Step 4
   (a) Steps 1 and Step 3 ($S_{DS} = 0.5$ g)
      i. End of Specimen – X Direction: The CDF curve at 60 kgf was consistently lower than at 150 kgf across all frequencies. Increasing T led to higher seismic energy at low frequencies ($\leq$ 10 Hz), attributed to enhanced potential energy storage in the cable. The overall ARMS at 150 kgf was 1.75 times higher than at 60 kgf.
      ii. End of Specimen – Y Direction: The CDF curve at 60 kgf was consistently lower than at 150 kgf. The overall ARMS at 150 kgf was 1.39 times higher than at 60 kgf.
      iii. Mid of Specimen – X Direction: The CDF curves at 60 kgf and 150 kgf were comparable, indicating that increased T stabilized the system due to the energy dissipation effect of the pulley friction damper.
      iv. Mid of Specimen – Y Direction: The CDF curve at 60 kgf was lower than at 150 kgf. The overall ARMS at 150 kgf was 1.20 times higher than at 60 kgf.
   (b) Steps 2 and Step 4 ($S_{DS} = 0.7$ g)
      i. End of Specimen – X Direction: The CDF curve at 60 kgf was larger than at 150 kgf across all frequencies. The overall ARMS at 150 kgf was 1.07 times lower than at 60 kgf.
      ii. End of Specimen – Y Direction: The CDF curve at 60 kgf was larger than at 150 kgf. The overall ARMS at 150 kgf was nearly equivalent to 60 kgf.
      iii. Mid of Specimen – X Direction: The CDF curve at 60 kgf was lower than at 150 kgf. Significant increases in seismic energy were observed at low frequencies (0–3 Hz) when T was increased to 150 kgf. The overall ARMS at 150 kgf was 4.71 times higher than at 60 kgf.
      iv. Mid of Specimen – Y Direction: The CDF curve at 60 kgf was lower than at 150 kgf. Significant increases in seismic energy were observed at low frequencies (0–3 Hz) when T was increased to 150 kgf. The overall ARMS at 150 kgf was 2.35 times higher than at 60 kgf.

(c) For Specimen 1:

i. For $S_{DS} = 0.5$ g: Increasing T from 60 kgf to 150 kgf resulted in a 1.54 times increase in seismic energy at the end, a 1.13 times increase at the mid, and an average increase of 1.30 times (see Fig. 16(e–g)).
ii. For $S_{DS} = 0.7$ g: Increasing T from 60 kgf to 150 kgf led to a 1.036 times increase at the end and a 3.16 times increase at the mid, with an overall average increase of 2.28 times (see Fig. 16(e–g)).

Increasing cable pre-tension enhances the stability of the novel system under low seismic intensity due to the energy dissipation effect of the pulley friction dampers. However, at high seismic intensity, the rise in cable pre-tension significantly amplifies seismic energy, particularly at the midpoints. This occurs because the increased pre-tension elevates the potential energy stored in the cable, which is quickly converted into kinetic energy during strong seismic events, intensifying the system's dynamic response. Additionally, higher pre-tension stiffens the cable and improves force transmission throughout the system, resulting in more seismic energy being transferred from the frame to the connectors, then to the cable, raceway, and lighting system. This effect is most pronounced at the midpoints, where potential energy changes are most significant, leading to the largest increases in kinetic energy. Consequently, the overall seismic energy within the system rises substantially under high seismic intensity, with the midpoints being particularly vulnerable to these effects.

4.5.3. Effect of support configurations

Based on the frequency domain analysis of Specimen 2, with both sub and main hangers, and Specimen 3, with only sub-hangers, both subjected to a simulated earthquake, the impact of hanger types on earthquake energy at $S_{DS} = 0.5$ g was analyzed (see Fig. 15(i–l) and Fig. 16(a–g)). The findings from comparing Specimen 2 (Step 1 -$T = 60$ kgf) and Specimen 3 (Step 5 -$T = 200$ kgf) are summarized as follows:

1. End of Specimen – X and Y Direction: The CDF curve of Specimen 2 was consistently lower than Specimen 3. Significant increases in seismic energy were observed at low frequencies (0–3 Hz). The overall ARMS of Specimen 3 was 3.38 and 4.58 times higher than Specimen 2 in the X and Y directions, respectively.
2. Mid of Specimen – X Direction: The CDF curve of Specimen 2 was similar to Specimen 3 at 0–10 Hz for X and 0–1 Hz for Y, but higher at frequencies above 10 Hz for X and larger than 1 Hz for Y. The overall ARMS of Specimen 2 was 1.536 and 2.85 times higher than Specimen 3 in the X and Y directions, respectively.
3. Based on Fig. 16 (e,f,g), without the main hanger and using $T = 200$ kgf, Specimen 3 showed an overall ARMS that was 2.86 times higher at the end and 2.13 times lower at the mid, with an overall average increase of 1.96 times compared to Specimen 2.

This finding illustrates the influence of support configurations on the seismic energy of structural systems. The results reveal that the absence of main hangers, combined with increased cable tension, significantly reduces seismic energy at the midpoint but introduces instability at the ends. These findings underscore the essential roles of hanger configuration and tension adjustments in controlling seismic energy, highlighting the importance of appropriate support design to enhance system resilience during earthquakes.

4.5.4. Effect of the fundamental frequencies

The TRS of the input acceleration peaks between 1 to 10 Hz in the X direction and 1 to 9 Hz in the Y direction, as shown in Fig. 8. Frequencies outside these ranges show decreased TRS values, suggesting that shifts in Specimen 2's fundamental frequencies significantly influence its earthquake energy.

Fig. 15(a-h) and Fig. 16(a-d) illustrate how variations in fundamental frequency, due to stiffness redistribution along Specimen 2 after each test step, lead to distinct changes in ARMS, reflecting trends in earthquake energy at both the end and middle positions. At the end position, the fundamental frequency in the X direction increased from 13.75 Hz to 15.5 Hz between Steps 1 and 3 ($S_{DS} = 0.5$ g), reducing ARMS from 0.449 to 0.326. A further increase to 15.5 Hz between Steps 2 and 4 ($S_{DS} = 0.7$ g) further reduced ARMS from 0.558 to 0.465. Conversely, at the middle position, the frequency decreased from 14 Hz to 12 Hz between Steps 1 and 3, increasing ARMS from 0.387 to 0.828. This trend continued from Step 2 to Step 4, with frequency dropping from 13 Hz to 12.5 Hz and ARMS rising from 0.709 to 0.825. These frequency shifts, driven by cumulative earthquake damage, significantly impacted spectral accelerations, altering the alignment with the TRS and leading to changes in seismic energy distribution across the system.

5. Conclusion

This study assessed the seismic performance of large-scale pulley wireway systems using biaxial shaking table tests under four consecutive earthquakes. A comparative analysis was conducted between novel pulley wireway systems and a conventional raceway lighting system of equal length. Four specimens were tested, including three pulley wireway systems and one conventional raceway system, each with varying suspended heights, support configurations, and cable pre-tension forces. The following key conclusions were drawn:

Table A.6
Accelerometer sensor location and orientation.

Description	Location	Direction	Remark
A1	Tabe A	X, Y	
A2	Top of stiff Frame A	X, Y	
A3	End of SP1	X, Y	
A4	End of SP2 (Step 1-4)	X, Y	End of SP3 in Step 5
A5	Middle of SP1	X, Y	
A6	Middle of SP2 (Step 1-4)	X, Y	Middle of SP3 in Step 5
A7	Middle of link segment 1	X, Y	
A8	Middle of link segment 2	X, Y	
A9	Tabe C	X, Y	

X: Longitudinal Y: Lateral.

1. The pulley wireway systems demonstrated superior earthquake performance compared to the conventional raceway lighting system, which failed after one earthquake event. The pulley systems remained functional through consecutive earthquakes with minimal maintenance.
2. Cumulative damage from successive earthquakes shifts the novel system's fundamental frequency along its length, altering its alignment with the ground motion response spectrum. These frequency shifts lead to corresponding changes in spectral accelerations throughout the system, significantly impacting its seismic response.
3. Lower suspension heights reduced lateral displacement responses but increased sensitivity to seismic activities, particularly at lower frequencies and higher intensities. Increased cable pre-tension improved stability at low seismic intensities but amplified seismic energy at high intensities, particularly at the midpoints.
4. Support configurations significantly influenced seismic responses. The presence of main hangers enhanced system stability, reducing relative lateral displacement and preventing instability at the system's ends. Conversely, the absence of main hangers, combined with increased cable tension, led to higher seismic energy and instability, particularly at the ends.
5. These findings underscore the critical role of suspension height, cable tension, and support configurations in optimizing the seismic resilience of pulley wireway systems. Balancing these parameters is essential for enhancing system performance under varying seismic intensities.

CRediT authorship contribution statement

Tran-Van Han: Writing – review & editing, Writing – original draft, Software, Methodology, Formal analysis, Data curation, Conceptualization. **Sung Chan Kim:** Writing – review & editing, Formal analysis. **Jiuk Shin:** Writing – review & editing, Formal analysis. **Nguyen Huu Cuong:** Writing – review & editing, Formal analysis. **Kihak Lee:** Writing – review & editing, Supervision, Resources, Project administration, Formal analysis.

Declaration of competing interest

The authors declare that they have no known competing financial interests or personal relationships that could have appeared to influence the work reported in this paper.

Data availability

The authors do not have permission to share data.

Acknowledgments

This study was completed with financial and technical assistance of Sehong Inc. Ltd located in Republic of Korea. This research was supported by Basic Science Research Program through the National Research Foundation of Korea (NRF) funded by the Ministry of Education (RS-2023-00247959).

Appendix

See Figs. A.17–A.20, Tables A.6–A.8.

Table A.7
LVDT location and orientation.

Description	Location	Direction	Remark
L1	Tabe A	X, Y	
L2	Top of stiff Frame A	X	
L4	End of SP1	X	
L6	Middle of SP1	Y	
L7	Middle of link segment 1	Y	

X: Longitudinal Y: Lateral.

Table A.8
Seismic parameters for required response spectrum.

Building code	Test criteria	S_{DS} (g)	z/h	Horizontal	
				A_{FLX-H} (g)	A_{RIG-H} (g)
IBC 2012	ICC-ESAC156	0.50	1.00	0.80	0.60

S_{DS}: Spectral response acceleration at short period
z/h: Height factor ratio.

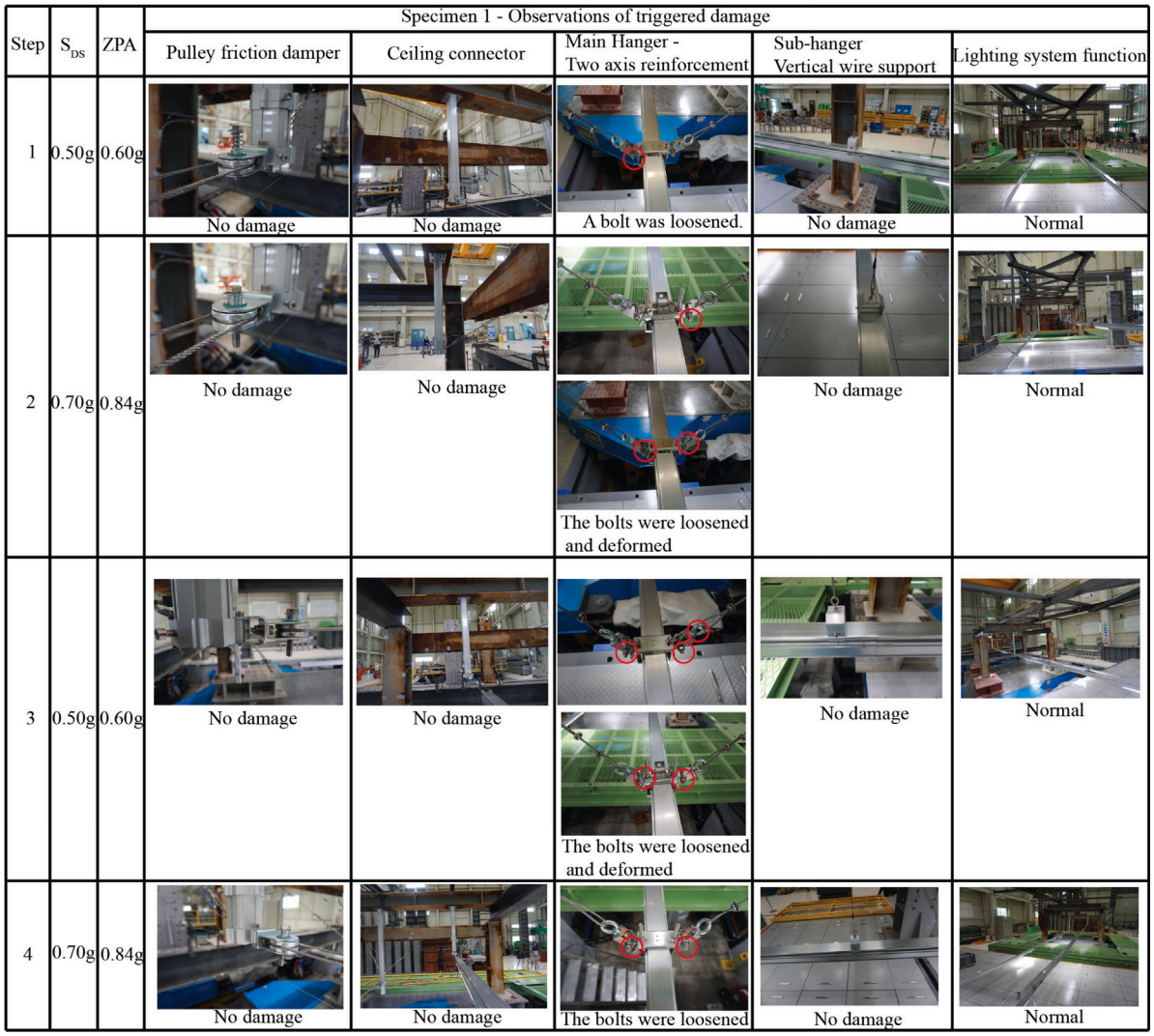


Fig. A.17. Observation of triggered damage to Specimen 1.

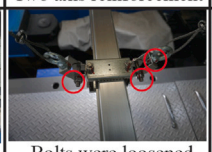
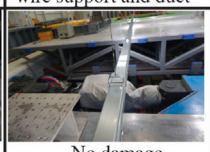
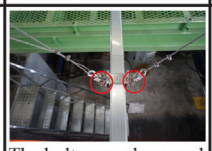
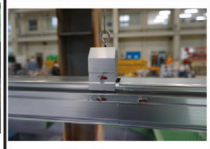
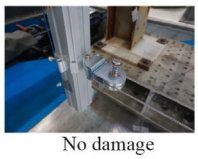
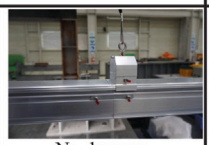
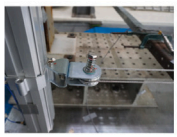
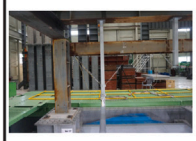
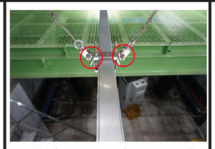
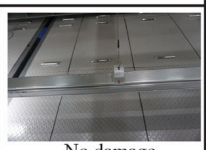
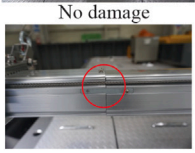
Step	S_{DS}	ZPA	Specimen 2 - Observations of triggered damage				
			Pulley friction damper	Ceiling connector	Main Hanger - Two axis reinforcement	Sub-hanger-Vertical wire support and duct	Lighting system function
1	0.50g	0.60g	 No damage	 No damage	 Bolts were loosened.	 No damage	 Normal
2	0.70g	0.84g	 No damage	 No damage	 The bolts were loosened and deformed	 No damage	 Normal
3	0.50g	0.60g	 No damage	 No damage	  The bolts were loosened and deformed	 No damage	 Normal
4	0.70g	0.84g	 No damage	 No damage	 Bolts were loosened.	 No damage  The connecting bolt between the two duct fell off	 Normal

Fig. A.18. Observation of triggered damage to Specimen 2.

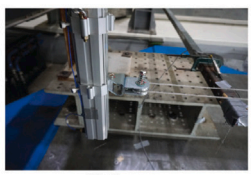
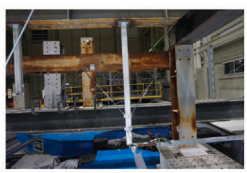
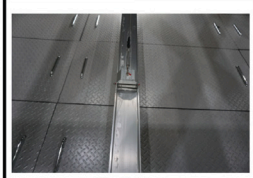
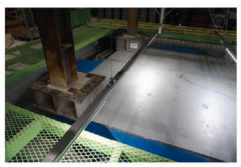
Step	S_{DS}	ZPA	Specimen 3 - Observations of triggered damage			
			Pulley friction damper	Ceiling connector	Sub-hanger-Vertical wire support and duct	Lighting function
5	0.5g	0.6g	 No damage	 No damage	 No damage	 No damage

Fig. A.19. Observation of triggered damage to Specimen 3.

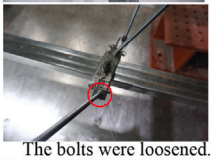
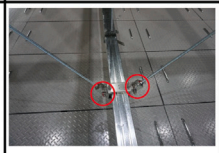
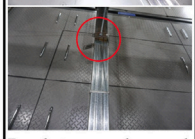
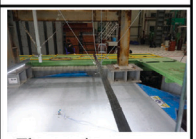
Step	S_{DS}	ZPA	Speciment 4 - Observations of triggered damage				
			Main Hanger - Three axis reinforcement	Main Hanger - Two axis reinforcement	Sub-hanger	Duct	Lighting function
5	0.50g	0.60g	  The bolts were loosened.		  Brackets were damaged	 A gap in the raceway unit was caused by the warping	 The specimen was damaged and warped

Fig. A.20. Observation of triggered damage to Specimen 4.

References

[1] P. FEMA, 58-2, Seismic Performance Assessment of Buildings Volume 2: Implementation Guide, Federal Emergency Management Agency, Washington, DC, USA, 2012.

[2] D. Perrone, P. Calvi, R. Nascimbene, E. Fischer, G. Magliulo, Seismic performance of non-structural elements during the 2016 central Italy earthquake, Bull. Earthq. Eng. 17 (2019) 5655–5677, http://dx.doi.org/10.1007/s10518-018-0361-5.

[3] Z. Luo, J. Xue, T. Zhou, L. Qi, X. Zhao, Shaking table tests and seismic design suggestions for innovative suspended ceiling systems with detachable metal panels, Eng. Struct. 232 (2021) 111830, http://dx.doi.org/10.1016/j.engstruct.2020.111830.

[4] C.A. Kircher, It makes dollars and sense to improve nonstructural system performance, in: Proc ATC 29-2 Seminar on Seismic Design, Performance, and Retrofit of …, 2003.

[5] A. Filiatrault, T. Sullivan, Performance-based seismic design of nonstructural building components: The next frontier of earthquake engineering, Earthq. Eng. Eng. Vib. 13 (1) (2014) 17–46, http://dx.doi.org/10.1007/s11803-014-0238-9.

[6] A.S. Gilani, A.M. Reinhorn, B. Glasgow, O. Lavan, H.K. Miyamoto, Earthquake simulator testing and seismic evaluation of suspended ceilings, J. Archit. Eng. 16 (2) (2010) 63–73, http://dx.doi.org/10.1061/(ASCE)1076-0431(2010)16:2(63).

[7] E. Miranda, G. Mosqueda, R. Retamales, G. Pekcan, Performance of nonstructural components during the 27 February 2010 Chile earthquake, Earthq. Spectra 28 (1_suppl1) (2012) 453–471, http://dx.doi.org/10.1193/1.4000032.

[8] D. Wang, J. Dai, Z. Qu, X. Ning, Shake table tests of suspended ceilings to simulate the observed damage in the M s 7.0 Lushan earthquake, China, Earthq. Eng. Eng. Vib. 15 (2) (2016) 239–249, http://dx.doi.org/10.1007/s11803-016-0319-z.

[9] L. Xiong, R. Lan, Y. Wang, X. Tian, B. Feng, Earthquake damage investigation of structures in 7.0 Lushan strong earthquake, J. Earthq. Eng. Eng. Vib. 33 (4) (2013) 35–43.

[10] K. Morita, M. Takayama, Behavior of seismically isolated buildings during the 2016 Kumamoto earthquakes, in: Proceedings of the NZSEE Conference, 2017, pp. 27–29.

[11] J. Rodgers, W. Hassan, C. Motter, J. Thornley, Impacts of the 2018 M7. 1 Anchorage earthquake on schools, Earthq. Spectra 37 (3) (2021) 1849–1874, http://dx.doi.org/10.1177/8755293020988022.

[12] Y. Tu, T. Yeh, Lessons learnt from buildings damaged in the 2018 Hualien earthquake, Taiwan.

[13] L. Qi, M. Kurata, Y. Ikeda, K. Kunitomo, M. Takaoka, Seismic evaluation of two-elevation ceiling system by shake table tests, Earthq. Eng. Struct. Dyn. 50 (4) (2021) 1147–1166, http://dx.doi.org/10.1002/eqe.3390.

[14] L. Qi, K. Kunitomo, M. Kurata, Y. Ikeda, Investigating the vibration properties of integrated ceiling systems considering interactions with surrounding equipment, Earthq. Eng. Struct. Dyn. 49 (8) (2020) 772–793, http://dx.doi.org/10.1002/eqe.3264.

[15] K.P. Ryu, A.M. Reinhorn, Experimental study of large area suspended ceilings, J. Earthq. Eng. 23 (6) (2019) 1001–1032, http://dx.doi.org/10.1080/13632469.2017.1342294.

[16] H.V. Tran, S.C. Kim, J. Shin, K. Lee, Shaking table testing of an innovative wireway vibration attenuation system, J. Constr. Steel Res. 197 (2022) 107477, http://dx.doi.org/10.1016/j.jcsr.2022.107477.

[17] H.V. Tran, S.C. Kim, J. Shin, K. Lee, Experimental study of a novel lighting support system reinforced with a pulley friction damper, J. Build. Eng. 52 (2022) 104385, http://dx.doi.org/10.1016/j.jobe.2022.104385.

[18] T.-V. Han, S.C. Kim, J. Shin, N.H. Cuong, K. Lee, Tri-axial shaking table testing of lighting support systems with pulley friction dampers and integrated dummy masses, Results Eng. 21 (2024) 101706, http://dx.doi.org/10.1016/j.rineng.2023.101706.

[19] E. ICC, AC156 acceptance criteria for seismic certification by shake-table testing of nonstructural components, 2010, International Code Council Evaluation Service, Country Club Hills, IL.

[20] J.L. Escalona, An analytical solution of the rope-sheave contact in static conditions based on a bristle model, Mech. Mach. Theory 185 (2023) 105334, http://dx.doi.org/10.1016/j.mechmachtheory.2023.105334.

[21] V.A. Lubarda, Determination of the belt force before the gross slip, Mech. Mach. Theory 83 (2015) 31–37, http://dx.doi.org/10.1016/j.mechmachtheory.2014.08.015.

[22] K. Lee, S. Ahn, D.-g. Hyun, T. Seo, Position prediction of viscoelastic rope on traction sheave with rope-slip model, Mech. Mach. Theory 180 (2023) 105131, http://dx.doi.org/10.1016/j.mechmachtheory.2022.105131.

[23] F.D. Guide, General magnaplate corporation, 1988, Linden, NJ, USA.

[24] W. Xie, E. De Meter, M. Trethewey, An experimental evaluation of coefficients of static friction of common workpiece–fixture element pairs, Int. J. Mach. Tools Manuf. 40 (4) (2000) 467–488, http://dx.doi.org/10.1016/S0890-6955(99)00082-6.

[25] SPS-F KOCED 0007-7419:2021, Shake-Table Testing Method for Seismic Performance Evaluation of Suspended Ceiling, 2021, Standard, Korea Construction Engineering Development Collaboratory Management Institute, Gyeonggi-do, ROK, 2021.

[26] F.A. Charney, Seismic Loads: Guide to the Seismic Load Provisions of ASCE 7-10, American Society of Civil Engineers, 2015.

[27] KCSC, Seismic design code of buildings (KDS 41 17 00), 2019, Sejong, Korea: Ministry of Land, Infrastructure and Transport.

[28] U.B. Code, International code council, 2000, Inc., Falls Church, VA, USA.
[29] O.S. Salawu, Detection of structural damage through changes in frequency: A review, Eng. Struct. 19 (9) (1997) 718–723, http://dx.doi.org/10.1016/S0141-0296(96)00149-6.
[30] F. FEMA, 461-Interim protocols for determining seismic performance characteristics of structural and nonstructural components through laboratory testing, Federal Emergency Management Agency (FEMA), Document No, 2007, Redwood City, CA.
[31] R.R. Craig Jr., A.J. Kurdila, Fundamentals of Structural Dynamics, John Wiley & Sons, 2006.
[32] MATLAB, Version 9.8.0 (R2020a), The MathWorks Inc., Natick, Massachusetts, 2020.
[33] H. Vold, J. Crowley, G.T. Rocklin, New ways of estimating frequency response functions, Sound Vib. 18 (11) (1984) 34–38.
[34] J. Wang, D. Lü, F. Jin, C. Zhang, Accuracy of the half-power bandwidth method with a third-order correction for estimating damping in multi-DOF systems, Earthq. Eng. Eng. Vib. 12 (1) (2013) 33–38.
[35] T. Irvine, The half power bandwidth method for damping calculation, 2005, http://www.vibrationdata.com. (Accessed: 17 August 2024).
[36] N.H. Dinh, S.-J. Lee, J.-Y. Kim, K.-K. Choi, Study on seismic performance of a mold transformer through shaking table tests, Appl. Sci. 10 (1) (2020) 361, http://dx.doi.org/10.3390/app10010361.
[37] Korean National Radio Research Agency, Earthquake Resistance Test. Method for Telecommunication Facilities, Korean National Radio Research Agency, 2015.
[38] P. Welch, The use of fast Fourier transform for the estimation of power spectra: a method based on time averaging over short, modified periodograms, IEEE Trans. Audio Electroacoust. 15 (2) (1967) 70–73, http://dx.doi.org/10.1109/TAU.1967.1161901.
[39] O. Solomon Jr., PSD Computations Using Welch's Method, NASA STI/Recon Technical Report N 92, 1991, p. 23584, URL https://www.osti.gov/servlets/purl/5688766.
[40] G. Housner, P.C. Jennings, Generation of artificial earthquakes, J. Eng. Mech. Div. 90 (1) (1964) 113–150, http://dx.doi.org/10.1061/JMCEA3.0000448.
[41] R. Simmons, Calulating grms (Root-Mean-Square Acceleration), 1997, URL https://femci.gsfc.nasa.gov/random/randomgrms.html.